Asymmetric apical domain states of mitochondrial Hsp60 coordinate substrate engagement and chaperonin assembly

AUTHORS: Julian R. Braxton[1-4], Hao Shao[2,3], Eric Tse[2,4], Jason E. Gestwicki[2,3,*], Daniel R. Southworth[2,4,*]

AFFILIATIONS:

[1]Graduate Program in Chemistry and Chemical Biology; University of California, San Francisco; San Francisco, CA 94158, USA

[2]Institute for Neurodegenerative Diseases; University of California, San Francisco; San Francisco, CA 94158, USA

[3]Department of Pharmaceutical Chemistry; University of California, San Francisco; San Francisco, CA 94158, USA

[4]Department of Biochemistry and Biophysics; University of California, San Francisco; San Francisco, CA 94158, USA

*Correspondence: jason.gestwicki@ucsf.edu; daniel.southworth@ucsf.edu

ABSTRACT:

The mitochondrial chaperonin, mtHsp60, promotes the folding of newly imported and transiently misfolded proteins in the mitochondrial matrix, assisted by its co-chaperone mtHsp10. Despite its essential role in mitochondrial proteostasis, structural insights into how this chaperonin binds to clients and progresses through its ATP-dependent reaction cycle are not clear. Here, we determined cryo-electron microscopy (cryo-EM) structures of a hyperstable disease-associated mtHsp60 mutant, V72I, at three stages in this cycle. Unexpectedly, client density is identified in all states, revealing interactions with mtHsp60's apical domains and C-termini that coordinate client positioning in the folding chamber. We further identify a striking asymmetric arrangement of the apical domains in the ATP state, in which an alternating up/down configuration positions interaction surfaces for simultaneous recruitment of mtHsp10 and client retention. Client is then fully encapsulated in mtHsp60/mtHsp10, revealing prominent contacts at two discrete sites that potentially support maturation. These results identify a new role for the apical domains in coordinating client capture and progression through the cycle, and suggest a conserved mechanism of group I chaperonin function.

INTRODUCTION:

Many proteins require the assistance of molecular chaperones to assume their native conformation(s) in the cell[1]. Chaperonins are an essential and highly conserved class of molecular chaperones found in all domains of life that form distinct multimeric ring complexes featuring a central cavity in which client protein substrates are folded[2,3]. Chaperonins are classified into two groups: group I members, including bacterial GroEL, form heptameric rings and require a co-chaperonin (here GroES) to completely seal the folding chamber, while group II members, including human TRiC/CCT, form octa- or nonameric rings and have helical insertions that close the chamber[4]. Both group I and II chaperonins play essential roles in protein homeostasis (proteostasis), likely because their architecture allows them to act on a wide variety of important client proteins.

Much has been learned about the mechanisms of group I chaperonins through pioneering studies of GroEL/ES[5]. Each GroEL promoter is composed of an apical domain, an intermediate domain, and an equatorial ATPase domain that coordinates inter-ring contacts to form the double-ring tetradecamer. In the intact heptamer, non-native client proteins bind tightly to exposed, inward-facing hydrophobic surfaces on GroEL apical domains, as well as to hydrophobic C-terminal tails found at the base of the folding cavity[6–9]. ATP binding to the equatorial domains induces an upward rotation and elevation of the apical domains, resulting in a decreased affinity for client and an increased affinity for GroES[10–13]. In this arrangement, GroES then binds the hydrophobic apical domain surfaces and seals the now-hydrophilic cavity, favoring the folding of the client protein[14–17]. GroES dissociates in a post-hydrolysis state, enabling the client to be released in a folded, native state or partially folded intermediate that requires subsequent rounds of chaperone interaction[18]. Through this mechanism, GroEL/ES promotes the folding of prokaryotic proteins and buffers cellular stress upon heat shock[19].

Mitochondrial heat shock protein 60 (mtHsp60) is the only group I chaperonin found in humans. Along with its co-chaperonin, mtHsp10, it promotes the folding of proteins newly imported into the mitochondrial matrix, as well as proteins that have become denatured upon thermal or chemical stress[20–22]. This chaperonin has been implicated in the progression of several cancers[23,24], and point mutations in mtHsp60 cause severe neurodegenerative diseases known as hereditary spastic paraplegias, which cause progressive muscle spasticity and lower limb weakness[25–29]. Because of these links to disease, there is interest in understanding the structure and function of mtHsp60/mtHsp10, and in developing inhibitors as chemical probes or potential therapeutics[30–33].

63   Given the structural and sequence homology between mtHsp60 and GroEL, the general

64   chaperone mechanisms are thought to be conserved[34]. Indeed, client-free structures of

65   mtHsp60 and mtHsp60/10 complexes confirm that several reaction intermediates in the

66   chaperone cycle are shared, however there are important differences in ring-ring assembly and

67   inter-ring allostery[35–38]. Moreover, there are multiple gaps in our structural and mechanistic

68   understanding of how mtHsp60/mtHsp10 binds and folds its clients during the ATP-dependent

69   reaction cycle. Advances in understanding mtHsp60 mechanism have been limited by the

70   relative instability of mtHsp60 complexes *in vitro*[39], likely explaining the lack of reported client-

71   bound mtHsp60 structures. Thus, it is not clear which regions of mtHsp60 might be involved in

72   these interactions or how clients might impact mtHsp60's structure. Additionally, in group I

73   chaperonins client and co-chaperone appear to bind to the same region[8], namely the inward-

74   facing hydrophobic apical domain helices H and I. It is therefore unclear how co-chaperonin

75   binding occurs with a bound client given these overlapping interactions. A possible explanation

76   comes from the observation that ATP binding decreases the affinity of GroEL for client: previous

77   studies have suggested the existence of a series of ATP-bound intermediates in which

78   chaperonin-client interactions are progressively weakened while chaperonin-co-chaperonin

79   interactions are strengthened[13,40–42]. These states might feature sufficiently low client off-rates

80   such that release is averted until co-chaperonin is bound. However, the structural details of such

81   complexes remain elusive.

82   We sought to determine the structural basis for progression through the nucleotide- and

83   mtHsp10-dependent mtHsp60 chaperone cycle using a disease-associated mutant that

84   increases oligomeric stability[26,28,43]. Cryo-EM structures of three mtHsp60 states in this cycle

85   were determined: apo-mtHsp60, ATP-bound mtHsp60, and ATP-bound mtHsp60/mtHsp10.

86   Unexpectedly, extensive sub-classification revealed low-resolution density corresponding to a

87   bound client in the chamber for each state. The position of client density appears coordinated by

88   distinct sites of interaction that include the apical domains, equatorial domain stem loops, and

89   disordered C-terminal tails. We identify a novel arrangement of ATP-bound mtHsp60 in which

90   the apical domains alternate between a client-contacting 'down' conformation and an outward-

91   facing 'up' conformation. The 'down' conformation allows contact with client but appears

92   incompatible with mtHsp10 binding, while the 'up' conformation is disengaged with client but has

93   accessible mtHsp10 binding sites. These results suggest a mechanism in which apical domain

94   up/down positioning enables client retention within the folding cavity to occur simultaneously

95   with mtHsp10 recruitment. The ATP-bound mtHsp60/mtHsp10 structure indicates that

96   subsequent movement of the remaining apical domains completes the contact with all mtHsp10

97   protomers, sealing the chamber and allowing folding to progress. We propose that this

98   mechanism may be conserved among group I chaperonins, including GroEL/ES, providing new

99   insight into how these chaperone machines are able to retain clients during recruitment of their

100   co-chaperonins.

101   **RESULTS:**

102   **The hereditary spastic paraplegia variant mtHsp60[V72I] forms stable heptamers and retains**

103   **significant chaperone activity**

104   Wild type mtHsp60 heptamers are unstable in the absence of mtHsp10 *in vitro*, and readily

105   dissociate into monomers at low concentration or temperature, or when incubated with

106   nucleotide[39], thereby complicating efforts to characterize the mtHsp60 chaperone cycle. To

107   facilitate structural studies of mtHsp60, we focused on the previously identified mtHsp60[V72I]

108   variant that is associated with hereditary spastic paraplegia SPG13[26,29], and is reported to have

109   increased oligomeric stability[43]. Residue V72 (numbering corresponds to the mature mtHsp60

110   protein after cleavage of the mitochondrial import sequence) is located in the equatorial domain

111   of mtHsp60 and packs into its hydrophobic core, but does not contact the ATP binding pocket

112   (Fig. 1a, Extended Data Fig. 1a). Importantly, the V72I mutation retains some client refolding

113   activity *in vitro*[43], suggesting that general features of the mtHsp60 chaperone cycle are

114   preserved.

115   To investigate the biochemical effects of the V72I mutation, we first confirmed the

116   increased stability of this mutant using size exclusion chromatography coupled to multi-angle

117   light scattering (SEC-MALS). This experiment revealed that the V72I mutant mostly remained as

118   heptamers, while wild-type protein had almost completely dissociated into monomers (Fig. 1b).

119   Importantly, incubation with ATP caused the complete dissociation of wild-type protein, while an

120   appreciable fraction remained oligomeric with the V72I mutation. Next, we analyzed the ATPase

121   activity of the V72I mutant *in vitro*. In the absence of mtHsp10, an increase in nucleotide

122   hydrolysis rate (~10 pmol ATP hydrolyzed/min for WT, ~21 for V72I) was observed (Extended

123   Data Fig. 1b), which is likely a result of the V72I protein's enhanced oligomerization (see Fig.

124   1b) and the known effect of cooperative ATP hydrolysis[44,45]. To determine if mtHsp10 could

125   further increase ATPase activity, we titrated with increasing concentrations of mtHsp10 and

126   found that it stimulated hydrolysis in both WT and V72I, although the activity in WT was higher

127   than in V72I at high mtHsp10 concentrations (~37 pmol/min for WT, ~31 for V72I at the highest

128   concentration tested). Overall, we conclude that the V72I mutation only modestly impacts ATP

129   hydrolysis. Next, to investigate client folding activity, we measured substrate turnover by

4

130 chemically denatured mitochondrial malate dehydrogenase (mtMDH) after incubation with the

131 mtHsp60/10 system using an established assay[46]. We identify that the V72I mutation impairs,

132 but does not eliminate, client refolding activity (initial velocity of mtMDH activity ~0.03 for WT,

133 ~0.02 for V72I) (Fig. 1c), indicating this mutant retains a significant amount of chaperone activity

134 *in vitro*. In sum, based on the modest biochemical effects that we and others identify, we

135 considered this mutation to be an attractive tool with which to structurally characterize the

136 chaperone states of mtHsp60.

Structures of mtHsp60^{V72I} heptamers reveal asymmetric apical domain conformations that coordinate a bound client

139 We first sought to determine cryo-EM structures of the nucleotide-free (apo) mtHsp60^{V72I}

140 heptamer. Reference-free two-dimensional (2D) class averages of the complex show top views

141 with clear heptameric rings and apparent C7 symmetry and side views with two bands of density

142 likely corresponding to the equatorial and apical domains (Fig. 1d, Extended Data Fig. 1c).

143 Remarkably, in certain top view class averages an additional asymmetric density in the central

144 cavity is observed that we hypothesized to be a bound protein client (Fig. 1d). Initial three-

145 dimensional (3D) classification of mtHsp60^{apo} particles reveal four prevalent classes (classes 1-

146 4) corresponding to mtHsp60 heptamers. Classes 2 and 4 feature density in the mtHsp60

147 central cavity, consistent with the top-view 2D averages (Extended Data Fig. 1d, Fig. 1d). In

148 total, ~39% of the particles selected from 3D classification contain this density. Given that

149 mtHsp60 heptamers are reconstituted from purified monomers and no additional protein was

150 carried through the purification (Extended Data Fig. 1e), we conclude the extra density is likely

151 partially folded mtHsp60 that is retained as a client in the chamber. Indeed, mtHsp60 is required

152 for its own assembly into oligomeric complexes in yeast mitochondria[47]. This serendipitous

153 observation indicates that the increased oligomer stability and slowed client folding activity of

154 V72I are features that combine to favor the capture of structures with bound client, making the

155 mtHsp60^{V72I} system poised to reveal the structural basis of mtHsp60 chaperone function.

156 Given the structural similarities between all mtHsp60 classes, we jointly refined particles

157 from all four classes with C7 symmetry enforced in order to improve resolution. This resulted in

158 a consensus map at 3.4 Å resolution, which enabled building of an atomic model (Fig. 1e,

159 Extended Data Fig. 2a, Table 1). All domains of mtHsp60 were modeled except the flexible C-

160 terminal tails, which were not resolved. This model highly resembles structures of previously

161 published mtHsp60 heptamers (Cα root mean squared deviation (RMSD) ~0.6-0.8 Å)[35,38]. While

162 the equatorial and intermediate domains are well-resolved in this map, density for the apical

5

163   domains, including the cavity-facing helices H and I, is considerably weaker, indicating flexibility

164   (Fig. 1f). This is also reflected in the higher *B*-factors relative to the equatorial and intermediate

165   domains (Extended Data Fig. 1f). Additional density in the central cavity is only observed at very

166   low thresholds, likely due to its heterogeneity and symmetry imposed during refinement. From

167   this analysis, we wondered whether the weaker apical domain density was a result of

168   independent apical domain motions of each protomer, or whether a series of discrete

169   heptameric arrangements of these domains existed, possibly related to client binding.

170   To better resolve the apical domains and potential client contacts we sorted mtHsp60

171   particles solely by apical domain conformation and client density, excluding signal from the

172   relatively invariant equatorial and intermediate domains. Given the C7 symmetry of the mtHsp60

173   heptamer, this was achieved by focused classification using symmetry-expanded[48] particles in

174   order to resolve symmetry-breaking conformations of apical domains (Fig. 1g). This approach,

175   and subsequent refinement of the entire volumes, resulted in two types of classes: those with

176   dramatically improved apical domain density, and those with strong density corresponding to

177   client (Extended Data Fig. 1d, 2b). The absence of strong client density in classes with well-

178   resolved apical domains is likely due to apical domain signal driving the classification, rather

179   than client. Inspection of the best class with improved apical domain density, termed mtHsp60^apo

180   focus, revealed a range of apical domain conformations around the heptamer, each related by a

181   rigid body rotation about the apical-intermediate domain hinge (Fig. 1h,i). Relative to the

182   consensus map, apical domains rotate both upward (i.e. away from the equatorial domain) and

183   downward; the range of rotation among all protomers spans ~10° (Fig. 1h,i, Extended Data Fig.

184   1g). Intriguingly, some of the largest differences in apical domain position occur in adjacent

185   protomers, giving rise to an apparent 'up' and 'down' alternating conformation (Fig. 1h,

186   protomers 7 through 3). In sum, we successfully resolved the flexible mtHsp60^apo apical

187   domains and identify that they adopt discrete up/down positions around the heptamer, rather

188   than being randomly oriented.

189   Client-containing maps from focused classification feature client at multiple locations in

190   the mtHsp60 heptamer (Fig. 1j, Extended Data Fig. 1d). Density corresponding to client is at an

191   overall low resolution compared to the mtHsp60 protomers, but this result is expected for a

192   partially folded protein that likely populates multiple conformations; low-resolution client density

193   has also been observed in GroEL structures[8,9,14,49]. In all structures, client is asymmetrically

194   positioned in the central cavity and contacts multiple mtHsp60 protomers, which is consistent

195   with the finding that group I chaperonins use multiple apical domains to engage client, and with

196   previous observations of asymmetric client density in GroEL tetradecamers[7–9]. However, there

197   are notable differences in client localization between the three classes, with density positioned

198   adjacent to the mtHsp60 apical domain, equatorial domain, or both. In the apical-only class

199   client density is proximal to helices H and I (Extended Data Fig. 1i), which contain multiple

200   hydrophobic residues shown to be critical for the binding of non-native proteins to GroEL[6], and

201   also form the surface engaged by mtHsp10[36,37]. Likewise, in the equatorial-only class client

202   density is located deeper in the central cavity and appears to interact with the disordered C-

203   terminal tails that project into this cavity (Extended Data Fig. 1j), and in the apical/equatorial

204   class both contacts are observed. Notably, all client-bound classes also feature asymmetric

205   apical domain conformations (Extended Data Fig. 1h), indicating that apical flexibility is a

206   general feature of mtHsp60[apo] and not limited to either client-bound or -unbound complexes.

207   **ATP binding induces mtHsp60 double ring formation and ordered apical domain**
208   **conformations**

209   We next sought to characterize apical domain conformations and client positioning in the

210   uncapped, ATP-bound state. ATP binding favors the formation of double-ring tetradecamers[50],

211   and reference-free 2D class averages of this sample indeed revealed a double ring

212   arrangement for the majority of particles, though top views of single rings were also observed

213   (Extended Data Fig. 3a). All top view averages show clear density corresponding to client, in

214   contrast to the weaker density in apo state particles, potentially indicating higher client

215   occupancy in the ATP sample (Extended Data Fig. 3a, 1c). Side view class averages show

216   markedly decreased apical domain resolution relative to that of the equatorial and intermediate

217   domains (Fig. 2a). Based on symmetric features of the complex identified in 2D analysis and the

218   lack of negative inter-ring cooperativity with respect to nucleotide binding in this system[50], we

219   refined the structure of the double-ring complex with D7 symmetry enforced (Fig. 2b, Extended

220   Data Fig. 3b). The resulting map has an overall resolution of 2.5 Å, with the highest resolution in

221   the equatorial and intermediate domains and greatly reduced resolution for the apical domains

222   due to their extended, flexible arrangement (Extended Data Fig. 2c, Table 1). This finding is

223   similar to the apo state, and indicates the equatorial and intermediate domains are

224   conformationally invariant, while the apical domains are substantially more flexible in the

225   uncapped, ATP state. Client appears as a diffuse central density at approximately the level of

226   the apical domains, and is likely less visible due to the imposition of symmetry. We built a

227   complete atomic model of this structure by fitting in a previous model of mtHsp60 and rigid body

228   docking the apical domain into the low-resolution density, followed by all-atom refinement

229 (Extended Data Fig. 3c). ATP is clearly resolved in the nucleotide binding pocket, indicating that

230 this structure corresponds to a pre-hydrolysis state (Extended Data Fig. 3d). As observed in

231 other chaperonins, nucleotide binding induces a downward ~20° rigid body rotation of the

232 intermediate domain over the equatorial nucleotide binding pocket, positioning the catalytic

233 aspartate (D397) in proximity to the ATP γ-phosphate (Extended Data Fig. 3e). The inter-ring

234 interface closely matches that of other nucleotide-bound mtHsp60 cryo-EM structures, with

235 protomers arranged in a staggered 1:2 conformation and presenting two possible sites of

236 interaction to the opposite ring[37]. At the first site, residues in helix P form polar and hydrophobic

237 interactions between rings, while no contacts are observed at the other site (Extended Data Fig.

238 3f). The mtHsp60 inter-ring interface is significantly reduced compared to those in analogous

239 GroEL complexes[10,11,51], likely explaining the ability of mtHsp60 to exist as single rings.

240 We postulated that the apical domains in the ATP state may be similarly positioned as

241 we identify in the apo state, adopting discrete up/down arrangements around the heptamer that

242 are potentially correlated with client contact. To investigate this possibility, we performed

243 focused classification of D7 symmetry expanded particles, using a mask that encompassed all

244 apical domains of one heptamer, and the central cavity (Fig. 2c, Extended Data Fig. 3b). Out of

245 50 classes, ten have greatly improved apical domain density for several protomers; the number

246 of protomers per heptamer with improved density varies between three and six. Intriguingly,

247 similar to the apo state, we identify an up/down arrangement in all apical domains with improved

248 resolution. Four of the ten classes (1-4) have six well-resolved apical domains in this pattern,

249 and the symmetry-breaking protomer (i.e. the protomer between an up and down protomer)

250 exhibits much weaker density, likely due to an inability to stably adopt either conformation.

251 Refinement of the best focused class with six well-resolved apical domains (class 1,

252 determined qualitatively) using a mask around the entire heptamer yielded the mtHsp60^{ATP}

253 focus map (Fig. 2d, Extended Data Fig. 2d, Table 1). This structure features substantially

254 improved density for six apical domains, while that of the symmetry-breaking protomer remained

255 more poorly resolved. Additionally, the equatorial and intermediate domains adopt identical

256 conformations as in the consensus structure, but two states of the apical domains, termed the

257 'up' and 'down' states, are observed in an alternating arrangement around the heptamer (Fig.

258 2e). With the improved apical domain resolution we identify that the up/down conformations are

259 related by a rigid body rotation of ~25°. The rotation of the 'up' apical domains displaces helices

260 H and I from the central cavity; this likely eliminates potential client binding to these helices. In

261 contrast, the rotation of the 'down' apical domains enables helices H and I to project directly into

8

262   the central cavity. Apical inter-protomer contacts between 'up' and 'down' protomers are

263   predominantly made using helices H and I, though the resolution is insufficient to identify

264   specific interacting residues (Extended Data Fig. 3g). Finally, modeling suggests that two

265   adjacent 'up' protomers would not significantly clash with each other but that two adjacent

266   'down' protomers would (Extended Data Fig. 3h). Given that adjacent 'up' protomers were not

267   observed during focused classification it therefore appears that the alternating up/down

268   arrangement is critical for stable apical domain positioning.

269   In addition to substantially improved apical domain density, the mtHsp60^{ATP} focus map

270   features asymmetric client density in the mtHsp60 central cavity (Fig. 2d). As in mtHsp60^{apo}

271   structures, client is contacted by the apical and equatorial domains (Fig. 2f-h). Apical contacts

272   are only made by 'down' protomers; this pattern of contact results in an asymmetric positioning

273   in the mtHsp60 cavity (Fig. 2d). Based on our molecular model, these interactions primarily

274   involve helix I and the underlying hydrophobic segment (Fig. 2g). The C-terminal tails and

275   equatorial stem loop (residue W42) also contact client, and, as in mtHsp60^{apo}, likely serve to

276   retain client in the folding cavity (Fig. 2h). This arrangement is distinct from the client densities

277   identified in the apo state, likely due to the rotation of all apical domains relative to those in apo

278   states. In sum, ATP binding induces a highly persistent alternating conformational arrangement

279   of mtHsp60 apical domains, which is identified in all classes with well-resolved apical domains.

280   This appears to cause a functional asymmetry in client binding ability and potentially enables

281   bifunctional interactions by apical domains.

282   **mtHsp10 binding symmetrizes mtHsp60 complexes and exposes distinct client-**

283   **contacting surfaces**

284   We next sought to determine structures of the mtHsp60-mtHsp10 complex in order to

285   investigate the active state for promoting client folding. To accomplish this, we incubated these

286   proteins with saturating ATP and prepared samples for cryo-EM as before. Reference-free 2D

287   class averages revealed predominantly symmetric double-ring complexes (hereafter referred to

288   as 'footballs' due to their resemblance to an American football), with a heptamer of mtHsp10

289   capping each mtHsp60 heptamer (Extended Data Fig. 4a,b). The structure of the football

290   complex with D7 symmetry imposed refined to a resolution of 2.7 Å, with well-resolved density

291   for mtHsp10 and all domains of mtHsp60, excluding the mtHsp60 C-terminal tails (Fig. 3a,

292   Extended Data Fig. 2e, Table 1). In contrast to the apo and ATP consensus structures, the

293   apical domains in this state are approximately as well-resolved as the equatorial and

294   intermediate domains. Client is only observed in this consensus map at very low thresholds,

295   likely due to partial occupancy in the central cavities of double-ring complexes and well-resolved

296   density for mtHsp60 and mtHsp10, which could overwhelm density for client. However, based

297   on previous structures we hypothesized that a subset of particles might contain stronger client

298   density.

299   To analyze the mtHsp10-bound state further, we built an atomic model of the football

300   complex (Extended Data Fig. 4c). ATP is well resolved in the nucleotide binding pocket, and

301   adopts the same orientation as in ATP-bound mtHsp60 (Fig. 3b). Likewise, the conformations of

302   the equatorial and intermediate domains are nearly identical to those in the ATP-bound state

303   (Extended Data Fig. 4d). Relative to the 'up' apical domains in mtHsp60^{ATP}, the apical domains

304   undergo a ~65° clockwise twist and elevation, generating a near-planar surface formed by

305   helices H and I onto which mtHsp10 docks. mtHsp10 predominantly interacts with these helices

306   through a hydrophobic triad (I31, M32, L33) in its mobile loop (Extended Data Fig. 4e). The

307   interior of the composite mtHsp60/10 folding cavity features increased hydrophilicity relative to

308   the interior of apo-mtHsp60 (Extended Data Fig. 4f), also a feature of GroEL/ES complexes[52].

309   Finally, the inter-ring interface of this complex very closely resembles that of uncapped

310   mtHsp60^{ATP} (Extended Data Fig. 4g).

311   To visualize client in football complexes, we performed focused classification using a

312   mask that included the folding cavity, with minimal density corresponding to mtHsp60 and

313   mtHsp10 (Fig. 3c, Extended Data Fig. 4b). This approach resulted in a class with significant

314   client density, which refined to 3.4 Å when using a mask encompassing the entire

315   mtHsp60/mtHsp10 ring (Fig. 3d). The bulk of the client density presents as a toroidal ring

316   approximately at the level of the mtHsp60 apical domains (Fig. 3d). mtHsp60-client contacts

317   become apparent when inspecting lowpass-filtered versions of the client density, which reveal

318   that in multiple mtHsp60 protomers, client contacts the interface of two alpha-helical hairpins,

319   which project two aromatic residues (F279, Y359) into the folding cavity (Fig. 3e,f). These

320   residues are only exposed to central cavity in the mtHsp10-bound state (Extended Data Fig.

321   4d). Contiguous density corresponding to client and the mtHsp60 C-terminal tails is also visible

322   in filtered maps, suggesting that these extensions play a role during client folding (Fig. 3g).

323   Overall, client localization and mtHsp60 contacts in this state resembles those in the

324   mtHsp60^{ATP} focus map and in client-bound GroEL/ES complexes[14,49], with both apical and

325   equatorial domains in contact with client. This arrangement is distinct from the mtHsp60^{apo} state,

326   which features several client topologies, including apical-only and equatorial-only contacts,

327   indicating a more heterogeneous association with mtHsp60^{apo} heptamers. Of note, multiple

10

328   distinct conformations in the mtHsp10-bound complex might exist, though the likely

329   heterogenous client population and sub-stoichiometric occupancy likely precludes the

330   identification of distinct, or folded, conformations.

331   **Client-contacting mtHsp60 residues are also important for oligomerization**

332   To probe the role of specific regions of mtHsp60 in client refolding activity, we selected four

333   aromatic residues observed to contact client and mutated them to Ala (Fig. 4a). W42 is located

334   on the equatorial domain stem loop, which is positionally invariant in all mtHsp60 states. Y201 is

335   located in the underlying segment of the apical domains, and was observed to contact client in

336   the ATP state. F279 and Y359 contact client in the mtHsp10-bound state due to a significant

337   rotation of the apical domain (Extended Data Fig. 4d); they do not face the folding chamber in

338   the apo or ATP-bound states. Conservation analysis between human mtHsp60 and its yeast

339   and bacterial orthologs revealed that three of these residues are conserved, while W42 is a Phe

340   in the other sequences (Fig. 4b). Analysis of ATPase activity in these mutants revealed that the

341   activity of three of the four, W42A, F279A, and Y359A, was not stimulated by mtHsp10 (Fig. 4c).

342   The activity of the Y201A mutant was modestly impaired at high concentrations of mtHsp10,

343   reminiscent of V72I (Extended Data Fig. 1b). Furthermore, all four mutants had impaired

344   mtMDH refolding activity compared to WT (Fig. 4d), a finding possibly explained by the

345   perturbed ATPase activity. Given the lack of mtHsp10-stimulated ATPase activity in three of four

346   mutants, we next wondered whether these mutations had altered oligomerization propensities.

347   Indeed, when analyzing these samples by SEC we observed that the W42A, F279A, and Y359A

348   mutants had completely dissociated into monomers, whereas WT and Y201A were at least

349   partly heptameric (Fig. 4e). Inspection of the apo mtHsp60 model revealed that F279 and Y359

350   are at an inter-protomer interface, and appear to contact the neighboring intermediate domain

351   (Fig. 4f). Thus, mutation of these two residues potentially impairs this interaction, leading to a

352   less stable heptamer. However, the mechanism of monomerization induced by the W42A

353   mutation, which is not proximal to any inter-protomer interface, is less clear. Together, we

354   conclude that client binding and oligomer assembly are somewhat coupled in the mtHsp60

355   system, making it difficult to assign distinct roles to these residues.

356   **A model of mtHsp60 client engagement and progression through the chaperone cycle**

357   The results presented here allow for the generation of a model describing client folding by the

358   mtHsp60-mtHsp10 system (Fig. 5, Supplementary Video 1). In this model, mtHsp60 without

359   nucleotide or co-chaperone exists as heptamers that are competent to bind client, with static

360   equatorial and intermediate domains and somewhat flexible apical domains loosely arranged in

11

361   alternating up/down conformations. The client folding chamber in the apo state allows for

362   multiple mtHsp60 interaction modes, including interaction with the inward surface of the apical

363   domains, the disordered C-terminal tails, or both. ATP binding induces the dimerization of

364   heptamers at the equatorial-equatorial interface, causes a downward rotation of the

365   intermediate domain, closing the nucleotide binding pocket, and causes apical domain rotation.

366   The apical domains of ATP-bound protomers are arranged in a strict up/down alternating

367   arrangement, with the 'down' protomers interacting with client through helix I and the underlying

368   hydrophobic segment. Equatorial interactions, namely with the C-terminal tail and an aromatic

369   residue projecting into the folding chamber, also contribute to client interaction. The 'up' ATP-

370   bound protomers likely provide an initial platform for mtHsp10 association, and interaction with

371   the remaining apical domains induces the transition into a fully symmetric conformation that

372   expands the now-capped folding chamber, allowing the client to fold. Finally, upon ATP

373   hydrolysis mtHsp10 dissociates from the heptamer, and client is released.

374   **DISCUSSION:**

375   Chaperonins are a superfamily of molecular chaperones that promote protein folding by

376   encapsulating unfolded or misfolded client proteins and allowing them to fold in a protected

377   environment. How client and co-chaperonin binding are coordinated to enable efficient client

378   folding in group I chaperonins, including the bacterial GroEL/ES and mitochondrial Hsp60/10

379   systems, has remained an active area of study. The mtHsp60/10 system is a relatively

380   understudied chaperonin homolog, yet has critical roles in human health and disease. Here we

381   used the stabilizing V72I mutant to structurally characterize intermediates in the mtHsp60

382   chaperone cycle, all of which unexpectedly contained client. These investigations substantially

383   increase our understanding of the mechanism of group I chaperonins.

384   In the apo state we identify that client contacts multiple mtHsp60 protomers in several

385   dynamic arrangements (Fig. 1j, Extended Data Fig. 1i,j), an observation consistent with previous

386   reports of multiple apical domains being necessary for efficient client binding in GroEL[7].

387   Intriguingly, though a preference for contact with contiguous protomers has been observed for

388   some clients, this does not appear to be the case upon ATP binding in the mtHsp60 system, as

389   apical domains of alternating protomers were observed to contact client (Fig. 2f). Therefore,

390   client interactions with chaperonins appear to change throughout the chaperone cycle.

391   Based on our structures we propose that apical domain asymmetry is a key feature of

392   the mtHsp60 cycle because it enables efficient client capture and retention. The mtHsp60 apo

393   state may be initially encountered by client and features moderate apical domain flexibility, in

394   agreement with other studies of mtHsp60 and its homologs[35,38,53]. We identify that apical

395   domains in intact heptamers exhibit loosely enforced alternating arrangements of 'up' and

396   'down' apical domains, rather than being randomly distributed (Fig. 1h,i). These arrangements

397   do not appear to be induced by client binding, as classes without resolved client that exhibit

398   these patterns were identified (Fig. 1i). It is therefore possible that these arrangements are

399   simply more energetically favorable than in a perfectly symmetric apical domain ring, perhaps

400   due to steric constraints. Intriguingly, similar apical domain arrangements are observed in ATP-

401   bound structures, though the degree of asymmetry is greater and the up/down pattern is

402   consistently observed across the different classes (Fig. 2f, Extended Data Fig. 3b). The

403   positioning in the apo state likely predisposes the apical domains for the alternating

404   arrangement we observed in the ATP-bound state. Moreover, the ATP dependence in mtHsp10

405   binding may be a consequence of increased stability of the upward-positioned apical domains to

406   facilitate binding. Notably, these results are in contrast to previous assumptions of symmetric

407   intermediates in the group I chaperonin cycle[10].

408   The alternating apical domain arrangement in the ATP-bound mtHsp60 state raises a

409   question about the role of the 7th protomer, located at the interface of 'up' and 'down' apical

410   domains. The apical domain of this protomer appears highly flexible, likely due to an inability to

411   adopt either ordered conformation, though two adjacent 'up 'protomers appear permitted

412   (Extended Data Fig. 3h) and are likely not observed due to the need for the stabilizing up/down

413   packing arrangement. Several possibilities exist as to the function of the 7th protomer: first, it

414   might play a role in co-chaperonin recruitment, enabling significantly greater access to helices H

415   and I and thus more efficient binding than even that facilitated by the three 'up' apical domains,

416   which are still somewhat inward-facing (Fig. 2d). Alternatively, it may be largely non-functional,

417   and the presence of the 7th protomer may merely serve to enlarge the size of the chaperonin

418   folding chamber, enabling encapsulation of larger clients. A final possibility is that this

419   symmetry-breaking protomer might confer a measure of stochasticity and dynamics in apical

420   domain conformation, possibly weakening the alternating ATP-bound arrangement, which could

421   enable efficient progression through the chaperone cycle. However, the evolution of octameric

422   group II chaperonins, despite having a distinct conformational cycle[54], indicates that

423   chaperonins with even numbers of protomers can be functional.

424   How client proteins are retained in the folding chamber during co-chaperonin binding has

425   remained an open question for all group I chaperonins. Here, the alternating apical domain

426   arrangements observed in the ATP-bound states raise exciting hypotheses about how this

13

427   objective is achieved. We speculate that the function of the 'up' apical domains is to enable

428   efficient recruitment of co-chaperonin, while the function of those in the 'down' conformation is

429   to interact with client. This alternating arrangement would enable simultaneous client retention

430   and co-chaperonin recruitment, likely preventing premature client release into solution during

431   co-chaperonin association. The three 'up' apical domains provide a platform for initial co-

432   chaperonin association (Fig. 5, green apical surfaces), and conformational rearrangements

433   cooperatively propagated throughout the entire heptamer result in apical domain rotations in all

434   protomers and the formation of the fully-encapsulated complex. This model is consistent with

435   previous biochemical studies of group I chaperonins, which suggested multiple ATP- and co-

436   chaperonin-bound intermediates on the pathway to complete encapsulation[13,41]. The structures

437   presented here are the first high-resolution views of an ATP-bound group I chaperonin without

438   co-chaperonin, leaving unclear whether other homologs such as GroEL function by the same

439   mechanism. However, given the high sequence similarity between members of the chaperonin

440   superfamily (Extended Data Fig. 5), it appears likely that the mechanism is conserved. Of note,

441   apical domains of apo GroEL exhibit considerably less flexibility than those in mtHsp60 and

442   have distinct inter-protomer interfaces[38], suggesting that a different mechanism may be

443   operative. The up/down apical domain configuration in ATP-bound protomers might also provide

444   an explanation of chaperonin-promoted folding without encapsulation observed in GroEL[55,56]:

445   the significant apical domain rotations relative to apo states may perform mechanical work on

446   clients, displacing them from the walls of the central chamber and promoting folding without the

447   need for the unique folding environment formed in the intact chaperonin-co-chaperonin

448   complex.

449   The oligomer disruption observed for several tested mtHsp60 mutants is striking, and

450   further confirms that mtHsp60 complexes are more labile than GroEL, which exists exclusively

451   as oligomers. Though it is presumed that equatorial contacts are largely responsible for

452   oligomeric stability in chaperonins[57], it appears that mutation of single equatorial and apical

453   domain residues in mtHsp60 is sufficient to impair oligomeric stability. Indeed, the causative

454   mutation of the hereditary spastic paraplegia MitCHAP-60[27], D3G, is characterized by a marked

455   decrease in oligomeric stability and thus chaperonin function[58], further supporting this instability

456   as a unique aspect of mtHsp60 function.

457   The function of single- vs double-ring states of group I chaperonins during their

458   chaperone cycles has been debated extensively[37,59–61]. In contrast to GroEL, apo mtHsp60

459   exists as single-ring heptamers, and in all other visualized states single-ring complexes are also

14

460   observed (Fig. 1, Extended Data Fig. 3a, 4b). A previously reported lack of inter-ring allostery

461   also suggests that single rings are functional[62], and it is thus tempting to speculate that double-

462   ring complexes are artefacts of the high protein concentrations employed *in vitro*. Indeed,

463   engineered single-ring variants of mtHsp60 have been demonstrated to support client folding *in*

464   *vitro*, strengthening this notion[37]. However, lack of direct high-resolution observation of mtHsp60

465   complexes *in situ* leaves this question unresolved. In sum, this work provides a comprehensive

466   view of the structural intermediates of mtHsp60 complexes, the conclusions from which are

467   potentially applicable to all group I chaperonins.

ACKNOWLEDGMENTS:

AUTHOR CONTRIBUTIONS:

473   J.R.B. cloned mtHsp60 mutants, expressed and purified proteins, performed biochemical and

474   cryo-EM experiments, built models, developed figures, and wrote and edited the manuscript.

475   H.S. expressed and purified proteins. E.T. operated electron microscopes and assisted with

476   data collection. J.E.G. and D.R.S. designed and supervised the project and wrote and edited the

477   manuscript.

DECLARATION OF INTERESTS:

479   The authors declare no competing interests.

480 **MAIN FIGURES:**

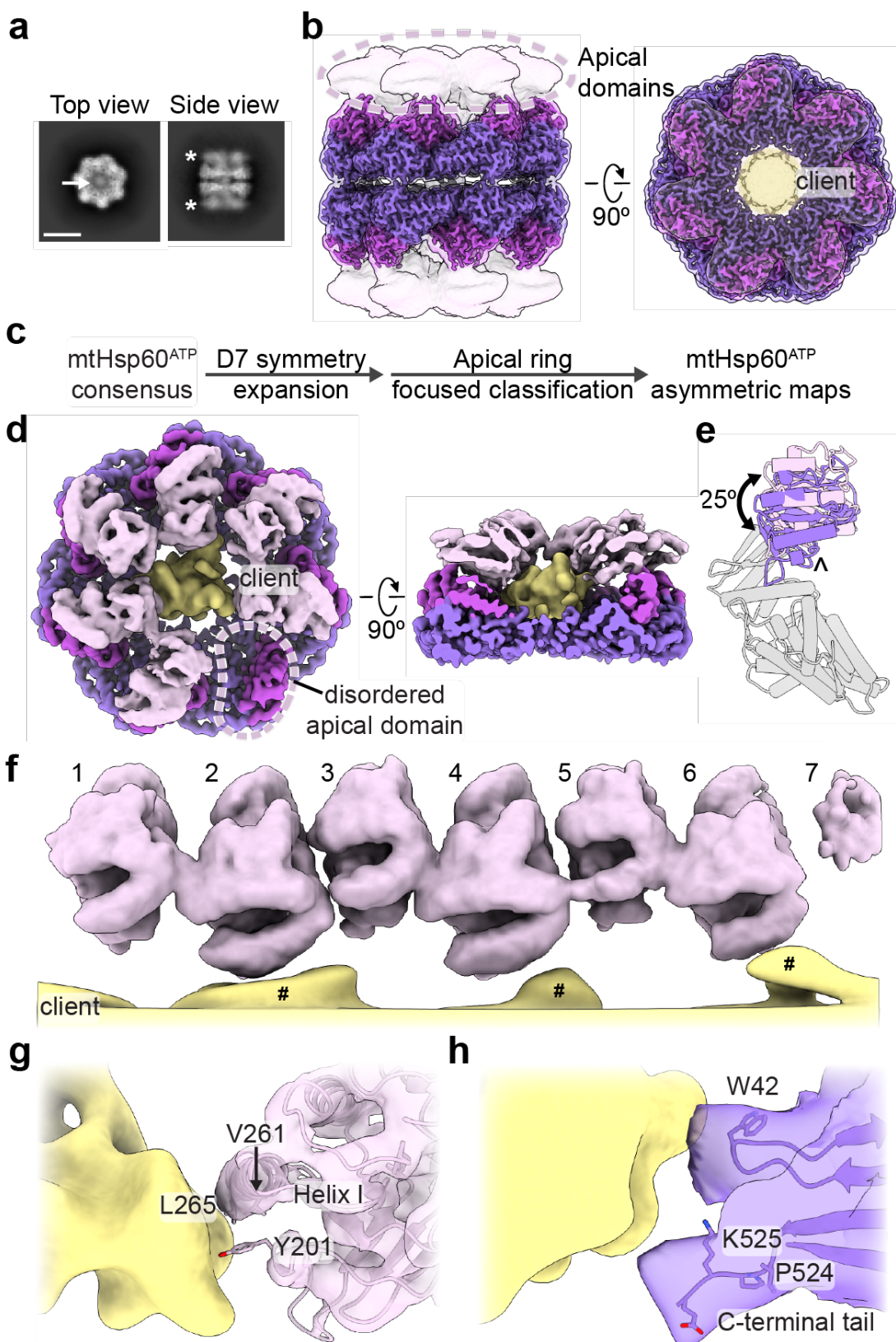Fig. 1
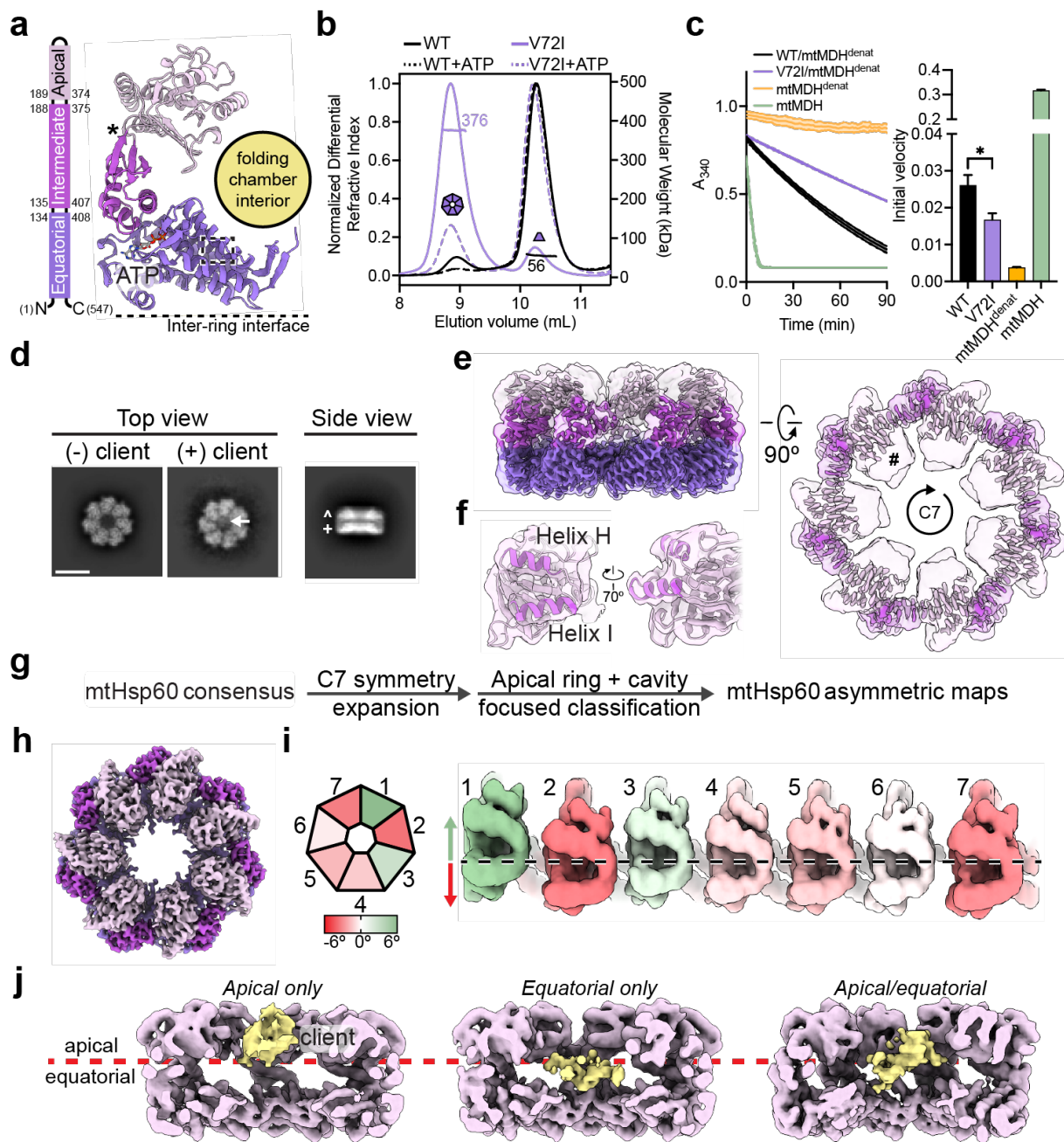
Fig. 1. Biochemical and structural analysis of the mtHsp60^{V72I} mutant

(**a**) Domain schematic and cartoon of an mtHsp60 protomer (ATP-bound consensus model). Location of the V72I mutation is indicated by a box, and the apical-intermediate domain hinge is marked (*). (**b**) SEC-MALS of mtHsp60 (black) and mtHsp60^{V72I} (purple) without ATP (solid lines) and with ATP (dashed lines). Normalized differential refractive index (left y-axis) vs elution volume (x-axis) are shown. The average molecular weight of the heptamer peak of mtHsp60^{V72I} and the monomer peak of mtHsp60 are shown and indicated by horizontal lines (kDa, right y-axis). (**c**) Enzymatic activity of chemically-denatured human mtMDH refolded by the mtHsp60-mtHsp10 system, as measured by the decrease in NADH (an mtMDH cofactor) absorbance at 340 nm (left panel, representative of three biological replicates). Dashed lines represent standard deviation of technical triplicates. Initial velocities of absorbance curves from three biological replicates are shown at right. Error bars represent standard error of the mean. *$p < 0.05$. Wild-type mtHsp60 (black) refolds mtMDH more efficiently than does V72I (purple). Native (green) and denatured mtMDH (mtMDH^{denat}) (orange) are shown for comparison. (**d**) Top and side view 2D class averages of client-bound and -unbound mtHsp60^{V72I} heptamers. Client is indicated with a white arrow. Equatorial (+) and apical (^) domains are indicated in the side view average. Scale bar equals 100 Å. (**e**) Overlay of the sharpened (opaque) and unsharpened (transparent) mtHsp60^{apo} consensus map, colored as in (**b**), showing high-resolution equatorial and intermediate domains and weak apical domain density. Lack of apical domain density in the sharpened map is indicated in the top view (#). (**f**) Detailed view of an apical domain from mtHsp60^{apo} consensus, with the sharpened map (opaque) overlaid with the unsharpened map (transparent) and the fitted model. Helices H and I (dark purple) are particularly poorly resolved, indicating flexibility. (**g**) Cryo-EM processing workflow to obtain maps with client and asymmetric apical domain conformations. (**h**) Top view of the sharpened mtHsp60^{apo} focus map, showing significantly improved apical domain features, colored as in (**b**). (**i**) (Left) heptamer cartoon showing apical domain rotation relative to the consensus map. Positive values (green) indicate an upward rotation (increasing equatorial-apical distance), negative values (red) indicate a downward rotation. (Right) unwrapped view of the apical domains of the unsharpened mtHsp60^{apo} focus map, showing significant asymmetry in apical domain conformations, labeled as in (**h**), colored as in the cartoon. Dashed line indicates the apical domain position in the consensus map. (**j**) Slabbed side views of unsharpened additional refinements from the classification outlined in (**g**), showing unannotated density likely corresponding to client (yellow) present in multiple conformations in the mtHsp60 heptamer (purple). A dashed line (red) delimits apical and equatorial regions of mtHsp60.

Fig. 2

a
Top view   Side view

b
Apical domains
client
−90°

c
mtHsp60^ATP consensus → D7 symmetry expansion → Apical ring focused classification → mtHsp60^ATP asymmetric maps

d
client
disordered apical domain
−90°

e
25°
∧

f
1 2 3 4 5 6 7
# # #
client

g
V261
L265   Helix I
Y201

h
W42
K525
P524
C-terminal tail

516

18

Fig. 2. ATP-induced mtHsp60^{V72I} conformational changes and client contacts

(**a**) Top and side view 2D class averages of ATP-bound mtHsp60^{V72I}. Arrow in top view indicates client density in folding cavity; asterisks in side view indicate poor apical domain resolution as compared to the equatorial and intermediate domains. Scale bar equals 100 Å. (**b**) Sharpened (opaque) and unsharpened (transparent) maps of consensus ATP-bound mtHsp60^{V72I}, colored as in Fig. 1. Note complete loss of apical domain density (encircled) in sharpened map. The central density corresponding to client is colored yellow in the top view. (**c**) Cryo-EM processing workflow to obtain maps with asymmetric apical domain conformations. (**d**) mtHsp60^{ATP} focus map, shown as unsharpened mtHsp60 density overlaid with segmented and 8 Å low-pass filtered client density. Note lack of density for one apical domain (encircled). (**e**) Models for representative 'up' (pink apical domain) and 'down' (purple apical domain) protomers, showing a rigid body rotation of the apical domain. Equatorial and intermediate domains are colored gray. The apical domain underlying segment (below helices H and I) is indicated (^). (**f**) Unwrapped view of the apical domains and client in the mtHsp60^{ATP} focus map, showing alternating up/down apical domain conformations, shown as in (**d**). Note that client extensions (#) are only proximal to 'down' protomers (2, 4, 6), and the weak apical domain density for protomer 7 at the symmetry-mismatched interface. (**g**) Client (shown as in (**d**)) contact with a representative 'down' apical domain (model overlaid with transparent unsharpened map). Putative client-contacting residue are shown. (**h**) Client (shown as in (**d**)) contact with a representative equatorial domain (filtered map). Putatively client-contacting residue Trp42 is shown, as are the last resolved residues of the C-terminal tail.

Fig. 3
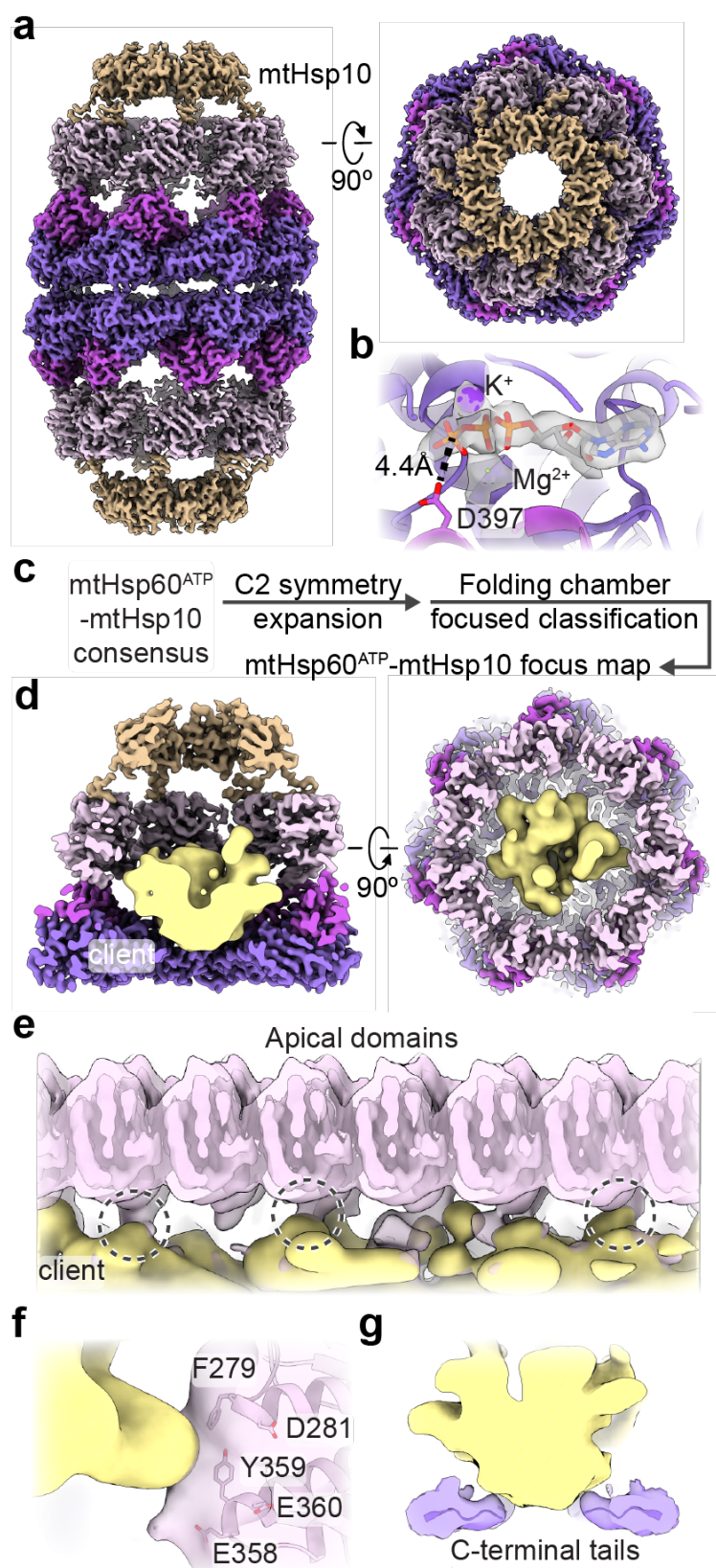
539 **Fig. 3. Analysis of mtHsp10-bound mtHsp60 complexes**

540 (**a**) Sharpened map of mtHsp60^{ATP}-mtHsp10, mtHsp60 colored as in Fig. 1, mtHsp10 in brown.

541 Note uniform quality of all mtHsp60 domains. (**b**) Nucleotide binding pocket of mtHsp60^{ATP}-

542 mtHsp10, showing density for ATP and the γ-phosphate thereof, and Mg^{2+} and K$^+$ ions (gray,

543 from sharpened map). (**c**) Cryo-EM processing workflow to obtain the mtHsp60^{ATP}-mtHsp10

544 focus map. (**d**) Slabbed views of mtHsp60^{ATP}-mtHsp10 focus map. mtHsp60/mtHsp10 density is

545 shown as the sharpened map, colored as in (**a**), client is shown as a segmented and 8 Å low-

546 pass filtered map. (**e**) Unwrapped view of the mtHsp60^{ATP}-mtHsp10 focus map, showing client

547 contact with multiple apical domains (encircled). mtHsp60 is shown as an unsharpened map

548 (pink, opaque) overlaid with an 8 Å low-pass filtered map, and client is shown as in (**d**). (**f**)

549 Enlarged view of client contact with a representative apical domain (both mtHsp60 and client

550 maps are low-pass filtered to 8 Å). Residues putatively involved in client contact are labeled. (**g**)

551 Enlarged view of client contact with the mtHsp60 C-terminal tails.
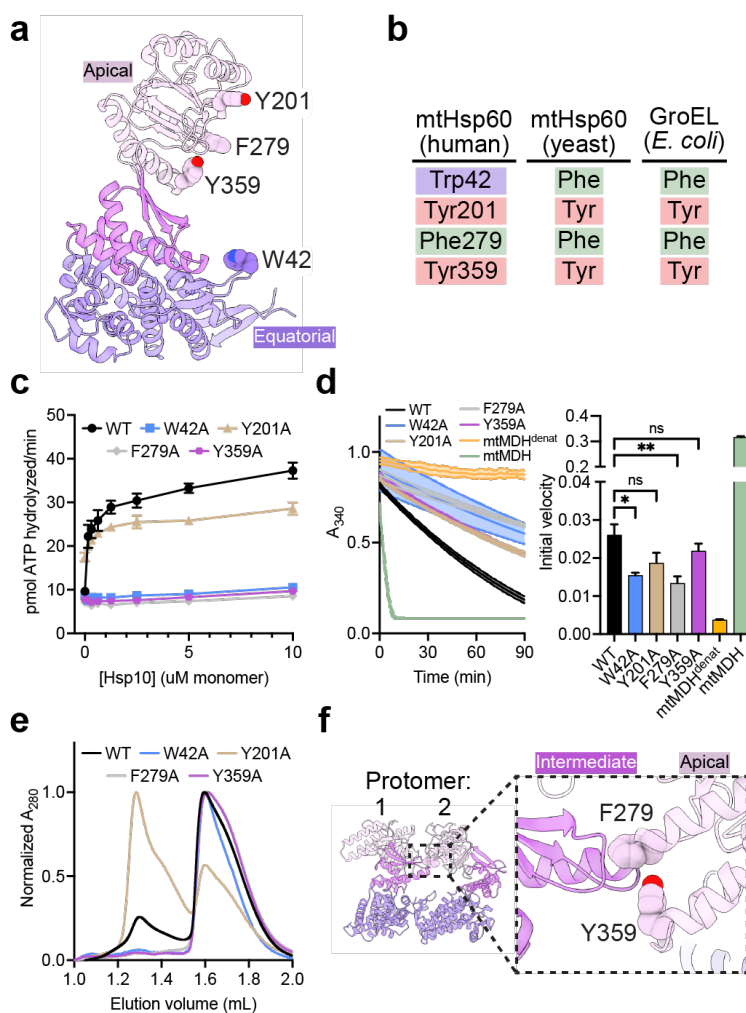
Fig. 4. Functional analysis of putative client-contacting mtHsp60 residues

(**a**) Protomer of mtHsp60 from mtHsp60^{ATP}-mtHsp10, showing residues mutated. (**b**) Conservation of residues in (**a**) among human and yeast mtHsp60 and GroEL. (**c**) Steady-state ATPase activity of mtHsp60 mutants vs concentration of mtHsp10. A representative experiment of three biological replicates is shown. Error bars represent standard deviation. (**d**) Enzymatic activity of chemically-denatured human mtMDH refolded by mtHsp60 mutants (left panel, representative of three biological replicates). Dashed lines represent standard deviation of technical triplicates. Initial velocities of absorbance curves from three biological replicates are shown at right. Error bars represent standard error of the mean. *p < 0.05, **p < 0.005, ns = not significant. (**e**) Analytical size exclusion chromatography traces of mtHsp60 mutants, showing complete monomerization of W42A, F279A, and Y359A mutants. (**f**) Model of two apo-mtHsp60 protomers, showing apical domain residues F279 and Y359 contacting the intermediate domain of an adjacent protomer.

Fig. 5
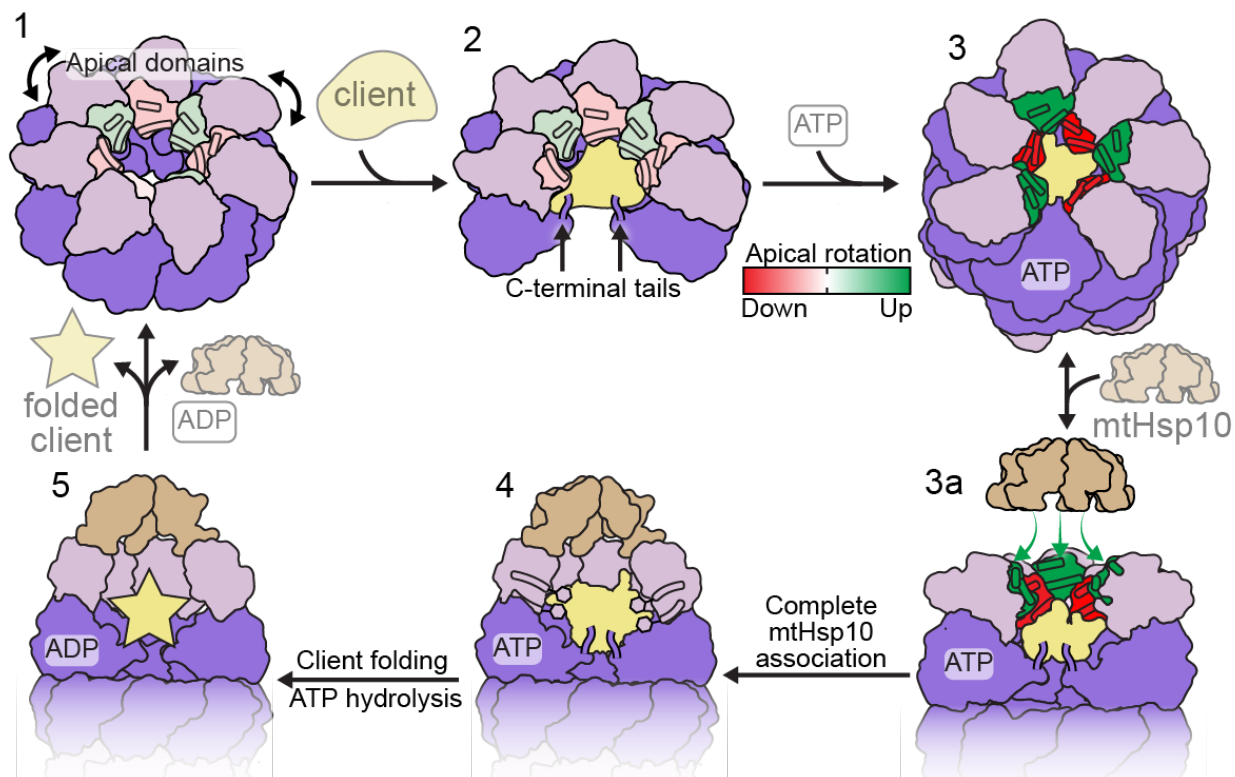
Fig. 5. Model of conformational changes in the client-engaged mtHsp60 reaction cycle

State 1: Apical domains (pink) of mtHsp60^{apo} heptamers are flexible, and exhibit modest rotation about the apical-intermediate hinge, denoted by coloration of helices H and I. State 2: Client binding to mtHsp60^{apo} preserves apical domain asymmetry, and client can localize to multiple depths of the heptamer, facilitated by mtHsp60 apical domains and the flexible C-terminal tails. State 3: ATP binding induces the dimerization of heptamers through the equatorial domains and a more pronounced apical domain asymmetry in an alternating up/down arrangement. Helices H and I in 'down' protomers (red) contact client, while those in 'up' protomers (green) are competent to bind mtHsp10. State 3a: mtHsp10 initially binds the mtHsp60 heptamer using the three upward-facing apical domains; all apical domains then transition to the conformation observed in the mtHsp10-bound complex (state 4). After ATP hydrolysis and client folding (state 5), client, mtHsp10, and ADP are released, and the double-ring complex disassociates into heptamers.

TABLES:

Table 1. Cryo-EM data collection, refinement, and validation statistics of mtHsp60 structures

	mtHsp60[apo] consensus (EMD-29813, PDB 8G7J)	mtHsp60[apo] focus (EMD-29814, PDB 8G7K)	mtHsp60[ATP] consensus (EMD-29815, PDB 8G7L)	mtHsp60[ATP] focus (EMD-29816, PDB 8G7M)	mtHsp60[ATP]-mtHsp10 consensus (EMD-29817, PDB 8G7N)	mtHsp60[ATP]-mtHsp10 focus (EMD-29818, PDB 8G7O)
Data collection and processing						
Microscope and camera	Glacios, K2	Glacios, K2	Glacios, K2	Glacios, K2	Glacios, K2	Glacios, K2
Magnification	53,937	53,937	53,937	53,937	53,937	53,937
Voltage (kV)	200	200	200	200	200	200
Data acquisition software	SerialEM	SerialEM	SerialEM	SerialEM	SerialEM	SerialEM
Exposure navigation	Image shift	Image shift	Image shift	Image shift	Image shift	Image shift
Electron exposure ($e^-/Å^2$)	66	66	66	66	66	66
Defocus range (μm)	-0.5 to -2.5	-0.5 to -2.5	-1.0 to -2.5	-1.0 to -2.5	-0.5 to -3.0	-0.5 to -3.0
Pixel size (Å)	0.927	0.927	0.927	0.927	0.927	0.927
Symmetry imposed	C7	C1	D7	C1	D7	C1
Initial particle images (no.)	970,545	970,545	696,761	696,761	113,390	113,390
Final particle images (no.)	839,799	192,680	405,263	137,145	81,840	37,628
Map resolution (Å)	3.4	3.8	2.5	3.2	2.7	3.4
FSC threshold	0.143	0.143	0.143	0.143	0.143	0.143
Map resolution range (Å)	2.5-8	3-6	2-6	2.5-8	2-7	2.5-8
Refinement						
Model resolution (Å)	3.6	4.1	2.7	3.4	2.8	3.6
FSC threshold	0.5	0.5	0.5	0.5	0.5	0.5
Map sharpening B factor ($Å^2$)	-221.8	-157.4	-127.9	-120.0	-120.6	-91.8
Model composition						
Nonhydrogen atoms	27,461	27,461	55,524	26,334	66,122	33,047
Protein residues	3,682	3,682	7,378	3,505	8,778	4,389
Ligands	0	0	42	21	42	7
B factors ($Å^2$)						
Protein	67.39	67.39	107.82	107.52	39.67	90.40
Ligand	N/A	N/A	23.99	44.80	11.75	61.26
R. m. s. deviations						
Bond lengths (Å)	0.015	0.014	0.008	0.004	0.004	0.003
Bond angles (°)	1.525	1.509	1.350	0.940	0.972	0.572
Validation						
MolProbity score	0.83	0.87	0.91	1.25	1.04	1.24
Clashscore	1.16	1.41	1.63	4.88	2.56	3.99
Poor rotamers (%)	0.00	0.00	0.79	0.00	0.20	0.00
Ramachandran plot						
Favored (%)	99.24	98.99	99.37	99.17	99.04	97.78
Allowed (%)	0.68	0.82	0.63	0.83	0.96	2.22
Disallowed (%)	0.08	0.19	0.00	0.00	0.00	0.00

585 **RESOURCE AVAILIBITY:**

586 **Materials availability:**

587 Requests for resources and reagents should be directed to Daniel R. Southworth

588 (daniel.southworth@ucsf.edu).

589 **Data availability:**

590 Cryo-EM densities have been deposited at the Electron Microscopy Data Bank under accession

591 codes EMD: 29813 (mtHsp60[apo] consensus), EMD: 29814 (mtHsp60[apo] focus), EMD: 29815

592 (mtHsp60[ATP] consensus), EMD: 29816 (mtHsp60[ATP] focus), EMD: 29817 (mtHsp60[ATP]-mtHsp10

593 consensus), and EMD: 29818 (mtHsp60[ATP]-mtHsp10 focus). Atomic coordinates have been

594 deposited at the Protein Data Bank under accession codes PDB: 8G7J (mtHsp60[apo]

595 consensus), PDB: 8G7K (mtHsp60[apo] focus), PDB: 8G7L (mtHsp60[ATP] consensus), PDB: 8G7M

596 (mtHsp60[ATP] focus), PDB: 8G7N (mtHsp60[ATP]-mtHsp10 consensus), and PDB: 8G7O

597 (mtHsp60[ATP]-mtHsp10 focus).

598 **METHOD DETAILS:**

599 **Molecular cloning**

600 The Q5 Site-Directed Mutagenesis kit (New England Biolabs) was used to introduce mutations

601 into the mtHsp60 expression construct.

602 **Protein expression and purification**

603 Human mtHsp60 constructs and mtHsp10 were expressed and purified as previously

604 described[39,46]. In brief, mtHsp60 variants ('mature' construct, residues 27-end) and full-length

605 mtHsp10 were cloned into pMCSG7, containing a TEV protease-cleavable N-terminal 6xHis tag.

606 pMCSG7-mtHsp60[WT], pMCSG7-mtHsp60[V72I], and pMCSG7-mtHsp10 were transformed into *E.*

607 *coli* BL21(DE3) chemically competent cells (New England Biolabs) using standard protocols.

608 BL21 cells were grown in Terrific Broth supplemented with 100 µg/ml ampicillin at 37 °C with

609 shaking until OD_{600} of ~1 was reached. Cultures were then induced with 400 µM isopropyl β-D-

610 1-thiogalactopyranoside (IPTG) and incubated at 37°C for 4 hours with shaking. Cells were

611 harvested by centrifugation for 10 minutes at 4,000 rpm, and stored at -80 °C until use.

612 All purification steps were performed at 4 °C unless otherwise specified. Cell pellets

613 were resuspended in His-binding buffer (50 mM Tris pH 8.0, 10 mM imidazole, 500 mM NaCl),

614 supplemented with EDTA-free protease inhibitor cocktail (Roche). The resuspensions were

615 homogenized by douncing and lysed by sonication. Lysates were clarified by centrifugation at

616 17,000 rpm for 30 min. Lysate supernatants were incubated with HisPur Ni-NTA resin (Thermo

617 Scientific) for 1 hour. The resin was washed with His-washing buffer (50 mM Tris pH 8.0, 30 mM

618 imidazole, 300 mM NaCl), and eluted with His-elution buffer (50 mM Tris pH 8.0, 300 mM

619 imidazole, 300 mM NaCl). The 6xHis tags were removed by incubating the elutions with TEV

620 protease and 1 mM DTT for 4 hours at room temperature, followed by overnight dialysis in SEC

621 buffer (50 mM Tris pH 7.7, 300 mM NaCl, 10 mM $MgCl_2$). The next day, uncleaved protein was

622 removed by a reverse nickel column and concentrated for reconstitution/size exclusion

623 chromatography. mtHsp10 heptamers were purified on a HiLoad 16/600 Superdex 200 pg

624 column (GE Healthcare) equilibrated in SEC buffer. mtHsp60 oligomers were reconstituted by

625 mixing mtHsp60 with KCl, Mg(OAc)$_2$ and ATP in the following ratio: 573 µL mtHsp60, 13 µL of 1

626 M KCl, 13 µL 1 M Mg(OAc)$_2$, and 52 µL 50 mM ATP. After incubation at 30 °C for 90 minutes,

627 the mixture was applied to the same SEC column, and the oligomeric fractions were collected,

628 supplemented with 5% glycerol, concentrated, flash frozen in liquid nitrogen, and stored at -80

629 °C.

630 The mtMDH bacterial expression vector was a gift from Nicola Burgess-Brown (Addgene

631 plasmid #38792; https://www.addgene.org/38792/). The vector was transformed into Rosetta

632 2(DE3)pLysS chemically competent cells (Novagen) using standard protocols. Rosetta 2 cells

633 were grown in Terrific Broth supplemented with 50 µg/ml kanamycin and 25 µg/ml

634 chloramphenicol at 37 °C with shaking until OD_{600} of ~1 was reached. Cultures were then

635 induced with 500 µM IPTG and incubated at 18°C overnight with shaking. Cells were harvested

636 by centrifugation for 10 minutes at 4000 rpm, and stored at -80 °C until use.

637 All purification steps were performed at 4 °C. A cell pellet was resuspended in mtMDH

638 His-binding buffer (50 mM HEPES pH 7.5, 20 mM imidazole, 500 mM NaCl, 5% glycerol),

639 supplemented with EDTA-free protease inhibitor cocktail (Roche). The resuspension was

640 homogenized by douncing and lysed by sonication. The lysate was clarified by centrifugation at

641 17,000 rpm for 30 min, filtered, and applied to a 5 mL HisTrap column (GE Healthcare). The

642 column was washed with 5 column volumes of mtMDH His-binding buffer, and eluted with a 10

643 column volume gradient of mtMDH His-elution buffer (50 mM HEPES pH 7.5, 250 mM

644 imidazole, 500 mM NaCl, 5% glycerol). Fractions containing mtMDH were concentrated and

645 injected onto a HiLoad 16/600 Superdex 200 pg column (GE Healthcare) equilibrated in mtMDH

646 SEC buffer (10 mM HEPES pH 7.5, 500 mM NaCl, 5% glycerol, 0.5 mM TCEP). Fractions

647 enriched in mtMDH were concentrated, flash frozen in liquid nitrogen, and stored at -80 °C.

648   Purity of all proteins was verified by SDS-PAGE and concentration was determined

649   using the Pierce BCA Protein Assay Kit (Thermo Scientific).

650   **SEC-MALS and analytical SEC**

651   For SEC-MALS, mtHsp60 samples (17 µM monomer) incubated with 1 mM ATP where

652   applicable were injected onto an SEC column (Shodex Protein KW-804) equilibrated at room

653   temperature in MALS buffer (20 mM HEPES pH 7.5, 100 mM KCl, 10 mM $MgCl_2$) connected to

654   an in-line DAWN HELEOS multi-angle light scattering detector and Optilab T-rEX differential

655   refractive index detector (Wyatt Technology Corporation). Molecular weights of proteins were

656   determined with the ASTRA V software package (Wyatt Technology Corporation). For analytical

657   SEC, mtHsp60 samples (17 µM monomer) were injected onto a Superdex 200 Increase 3.2/300

658   column equilibrated at room temperature in MALS buffer.

659   **BIOMOL Green ATPase assay**

660   ATPase activity was measured in 96-well plates using an assay reported previously[75], with

661   minor modifications. In brief, 500 nM mtHsp60 monomer (final) was incubated with a two-fold

662   dilution series of mtHsp10, starting at 10 uM monomer (final), in ATPase buffer (100 mM Tris pH

663   7.4, 20 mM KCl, 6 mM $MgCl_2$, 0.01% Triton X-100). ATP was added to 1 mM (final), and the

664   reactions (25 µL total) were incubated for 1 hour at 37 °C. After incubation, 80 µL of BIOMOL

665   Green reagent (Enzo Life Sciences) was added to each well, immediately followed by 10 µL of

666   32% w/v sodium citrate, to limit nonenzymatic hydrolysis of ATP. The reactions were mixed and

667   incubated at 37 °C for 15 minutes, and then A_{620} was measured on a SpectraMax M5 (Molecular

668   Devices). ATP hydrolysis (pmol ATP hydrolyzed/min) was quantified using a standard curve of

669   sodium phosphate and the following equation:

670    $$\text{pmol ATP hydrolyzed/min} = \frac{A_{620} \times \text{reaction volume (µL)}}{\text{slope of standard curve} \left(A_{620} / \mu\text{M phosphate} \right) \times \text{incubation time (min)}}$$

671   **mtMDH refolding assay**

672   mtMDH activity after refolding by mtHsp60/10 was measured using a previously reported assay

673   with minor modifications[46]. To prepare chemically denatured mtMDH (mtMDH^{denat}), mtMDH was

674   incubated for 1 hour at room temperature in denaturant buffer (50 mM Tris pH 7.4, 6 M

675   guanidine HCl, 10 mM DTT). A binary complex of mtHsp60-mtMDH^{denat} was prepared by adding

676   mtMDH^{denat} (120 nM final) to mtHsp60 (3.33 µM final) in mtMDH reaction buffer (50 mM Tris pH

677   7.4, 20 mM KCl, 10 mM $MgCl_2$, 1 mM DTT), and incubating for 10 minutes at room temperature.

27

678 mtHsp10 (6.67 µM final) was added to this mixture, and 30 µL aliquots were transferred to 96-

679 well plates in triplicate. 20 µL ATP was added to each well (1 mM final), and reactions were

680 incubated at 37 °C for 1 hour. After incubation, an equivalent amount of mtMDH or mtMDH^{denat}

681 was added to the plate as controls for mtMDH activity, and 10 µL of 500 mM EDTA pH 8.0 was

682 added to all wells to quench mtHsp60-mediated refolding. 20 µL of mtMDH enzymatic reporter

683 (2.4 mM NADH, 20 mM sodium mesoxalate dissolved in mtMDH reaction buffer, freshly

684 prepared for each assay) was added to all wells, and A_{340} was measured by a SpectraMax M5

685 (Molecular Devices) for 90 minutes at room temperature. Initial velocities of NADH oxidation

686 were calculated using the following equation:

687
$$\text{Initial velocity } (\frac{A_{340}}{\text{min}})=-1\times \frac{A_{340_{t=3\text{ min}}}-A_{340_{t=0\text{ min}}}}{3\text{ min}}$$

688 Significance testing for calculated initial velocities was performed using Dunnett's multiple

689 comparison test, using mtHsp60^{WT} as the control.

690 **SDS-PAGE analysis**

691 mtHsp60^{V72I} (10 µL of 5 µM monomer) was loaded on a 4-15% TGX gel (Bio-Rad), run for 30

692 min at 200 V, and stained using Coomassie Brilliant Blue R-250 (Bio-Rad).

693 **Cryo-EM sample preparation, data collection, and image processing**

694 For apo mtHsp60 samples, 2.4 mg/mL mtHsp60 was prepared in ATPase buffer (without

695 detergent), supplemented with 0.1% n-Octyl-beta-D-glucopyranoside (Alfa Aesar) to improve

696 particle orientation distribution. For samples with ATP, 0.2-0.6 mg/mL mtHsp60 was prepared in

697 ATPase buffer (without detergent), supplemented with 1 mM ATP. For samples with mtHsp10,

698 6.3 mg/mL mtHsp60 and 1.3 mg/mL mtHsp10 were prepared in ATPase buffer, supplemented

699 with 1 mM ATP and 0.1% amphipol A8-35 (Anatrace) to improve particle orientation distribution.

700 3 µL of each sample was applied to glow-discharged (PELCO easiGlow, 15 mA, 2 min) holey

701 carbon grid (Quantifoil R1.2/1.3 on gold or copper 200 mesh support), blotted for 3 seconds with

702 Whatman Grade 595 filter paper (GE Healthcare), and plunge frozen into liquid ethane cooled

703 by liquid nitrogen using a Vitrobot (Thermo Fisher Scientific) operated at 4 or 22 °C and 100%

704 humidity. Samples were imaged on a Glacios TEM (Thermo Fisher Scientific) operated at 200

705 kV and equipped with a K2 Summit direct electron detector (Gatan). Movies were acquired with

706 SerialEM[63] in super-resolution mode at a calibrated magnification of 53,937, corresponding to a

707 physical pixel size of 0.927 Å. A nominal defocus range of -1.0 to -2.0 µm was used with a total

708 exposure time of 10 sec fractionated into 0.1 sec frames for a total dose of 66 e$^-$/Å^2 at a dose

709   rate of 6 e⁻/pix/s. Movies were subsequently corrected for drift, dose-weighted, and Fourier-

710   cropped by a factor of 2 using MotionCor2[64].

711   For the apo-mtHsp60 dataset, a total of 20,223 micrographs were collected over two

712   different sessions and initially processed in cryoSPARC[67]. After Patch CTF estimation,

713   micrographs were manually curated to exclude those of poor quality, followed by blob- or

714   template-based particle picking, 2D classification, and *ab initio* modeling in cryoSPARC.

715   Datasets were processed separately through 2D classification, and particles selected from 2D

716   analysis were subjected to an initial 3D classification in Relion[68]. Four classes resembled

717   mtHsp60 heptamers, some of which contained density in the central cavity likely corresponding

718   to a bound client. The particles from these four classes were jointly refined in cryoSPARC with

719   C7 symmetry imposed. This resulted in the mtHsp60^{apo} consensus map, which featured well-

720   resolved equatorial and intermediate domains but very poor density for the apical domains. To

721   improve the resolution of the apical domains and resolve client, particles from this refinement

722   were symmetry expanded in C7 and subjected to focused classification without image alignment

723   (hereafter referred to as skip-align classification), using a mask encompassing all apical

724   domains and the central cavity. This resulted in a number of classes with significantly improved

725   apical domains in asymmetric conformations (for example, class 1), as well as a number of

726   classes with moderate apical domain resolutions but strong density corresponding to client

727   (classes 2-4). Particles from each of these classes were re-extracted and locally refined to

728   obtain the entire structure.

729   For the mtHsp60/ATP dataset, a total of 15,900 micrographs were collected over three

730   different sessions, and initially processed as for apo-mtHsp60, leaving particles from different

731   collections separate until initial 3D classification in Relion. Two classes from this job, both

732   double-ring tetradecamers with weak central density corresponding to client, were jointly refined

733   in cryoSPARC with D7 symmetry enforced, yielding the mtHsp60^{ATP} consensus map. As for the

734   mtHsp60^{apo} consensus map, the equatorial and intermediate domains were well-resolved in this

735   map, but density for the apical domains was extremely poor, indicating significant

736   conformational flexibility. To better resolve the apical domains, skip-align focused classification

737   was performed on D7-symmetry expanded particles, using a mask that encompassed the apical

738   domains of 1 heptamer. This yielded many classes with between three and six ordered apical

739   domains, with the remainder of the apical domains being poorly resolved. Local refinement in

740   cryoSPARC of the best class (class 1) yielded the mtHsp60^{ATP} focus map.

741   For the mtHsp60/mtHsp10/ATP dataset, a total of 7,460 micrographs were collected

742 across two different sessions, and initially processed as for apo-mtHsp60, leaving particles from

743 different collections separate until initial 3D classification in Relion. Two classes from this job,

744 both resembling double-ring complexes with each ring bound by mtHsp10, were jointly refined in

745 cryoSPARC with D7 symmetry imposed, resulting in the mtHsp60^{ATP}-mtHsp10 consensus map.

746 Weak density in the central cavities prompted further analysis to classify rings with and without

747 client density. To this end, a mask was created encompassing the folding chamber of one ring,

748 with minimal density for mtHsp60 or mtHsp10. A skip-align focused classification into two

749 classes was performed in Relion on C2-symmetry expanded particles, which resulted in classes

750 with and without client density. The class with client was locally refined in cryoSPARC using a

751 mask that encompassed the entire ring, resulting in the mtHsp60^{ATP}-mtHsp10 focus map.

Molecular modeling

753 For the mtHsp60^{apo} consensus structure, a previously published model (PDB 7AZP) was docked

754 and refined against the sharpened map using Rosetta Fast Torsion Relax. The V72I mutations

755 were made using Coot[70]. This model was then refined against the sharpened mtHsp60^{apo} focus

756 map. For the mtHsp60^{ATP} consensus structure, a chain from a previously published model (PDB

757 6MRC) was docked into an asymmetric unit of the unsharpened map, and the apical domain

758 was rigid-body docked using Phenix Real Space Refine[72]. The V72I mutation and ligand

759 modifications were then made in Coot, followed by generation of the complete 14-mer in Phenix

760 and refinement against the sharpened map using Phenix Real Space Refine. One heptamer

761 from this model was docked into the sharpened mtHsp60^{ATP} focus map, and refined using

762 Phenix Real Space Refine. The disordered apical domain was omitted from the model due to

763 extremely poor resolution. For the mtHsp60^{ATP}-mtHsp10 consensus structure, a protomer pair of

764 mtHsp60-mtHsp10 from a previously published model (PDB 6MRC) was docked into an

765 asymmetric unit of the sharpened map. The V72I mutation and ligand modifications were then

766 made in Coot, followed by generation of the complete 14-mer in Phenix and refinement against

767 the sharpened map using Phenix Real Space Refine. One ring of this model was then docked

768 into the sharpened mtHsp60^{ATP}-mtHsp10 focus map, and refined using Phenix Real Space

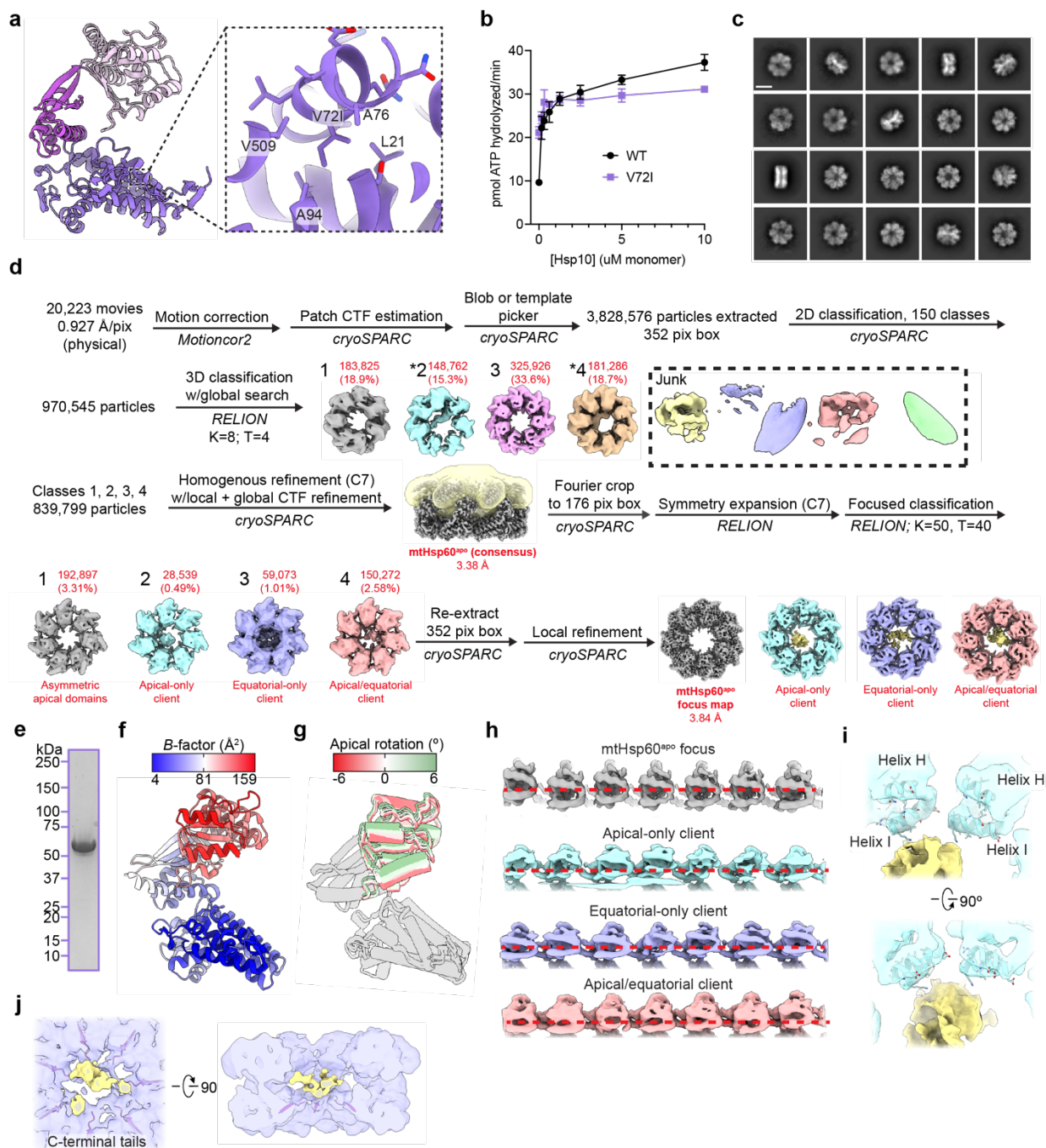769 Refine. Coot, ISOLDE[69], and Phenix were used to finalize all models.

Data analysis and figure preparation

771 Biochemical data was analyzed and plotted using Prism 9.3.1 (GraphPad). Figures were

772 prepared using Adobe Illustrator, UCSF Chimera, and UCSF ChimeraX[73,74].
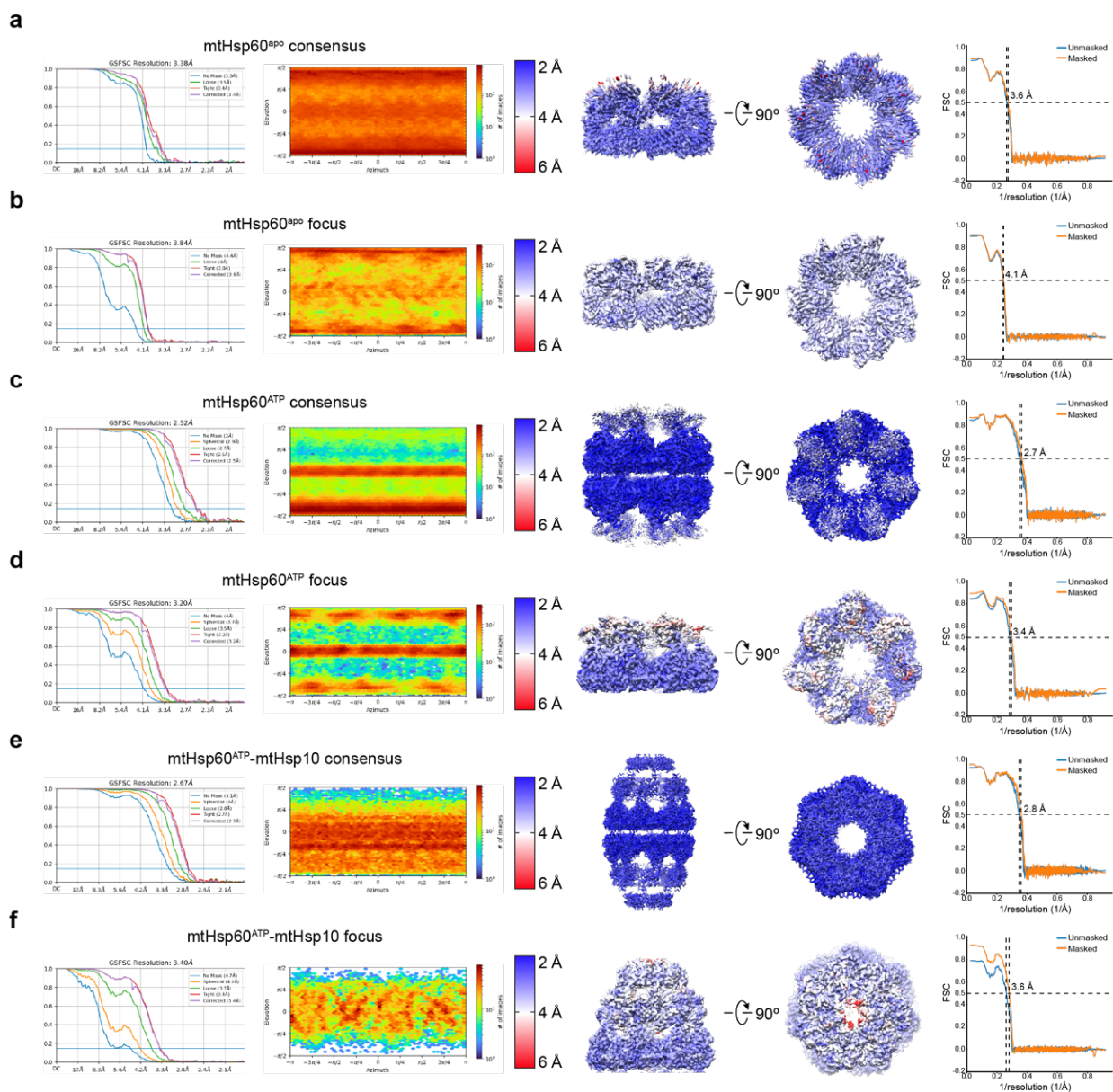
773 **EXTENDED DATA:**

Extended Data Fig. 1

774

31

Extended Data Fig. 1. Biochemical and cryo-EM analysis of apo mtHsp60^{V72I}

(**a**) View of V72I mutation in mtHsp60^{apo}, colored as in Fig. 1b. Adjacent hydrophobic residues also labeled. (**b**) Steady-state ATPase activity of mtHsp60 (black) and mtHsp60^{V72I} (purple) as a function of mtHsp10 concentration. A representative experiment of three biological replicates is shown. Error bars represent standard deviation. (**c**) Representative 2D class averages from the mtHsp60^{apo} dataset. Scale bar equals 100 Å. (**d**) Cryo-EM processing workflow for structures obtained from the mtHsp60^{apo} dataset. The mask used for focused classification is shown in transparent yellow with the consensus map. Client-containing maps from the initial 3D classification are indicated (*). (**e**) Coomassie Brilliant Blue-stained SDS-PAGE gel of recombinant mtHsp60^{V72I}, showing no strong additional bands corresponding to other proteins. (**f**) Protomer of apo mtHsp60 consensus colored by *B*-factor. (**g**) Overlay of mtHsp60^{apo} focus protomers, with apical domains colored as in Fig. 1i. (**h**) Unwrapped views of unsharpened mtHsp60^{apo} focus and client-bound maps, showing apical domain asymmetry. Horizontal red dashed lines are for clarity. (**i**) Enlarged view of apical domain helices H and I from the mtHsp60^{apo} apical-only client map. (**j**) Enlarged view of resolved portions of C-terminal tails from the mtHsp60^{apo} equatorial-only client map.
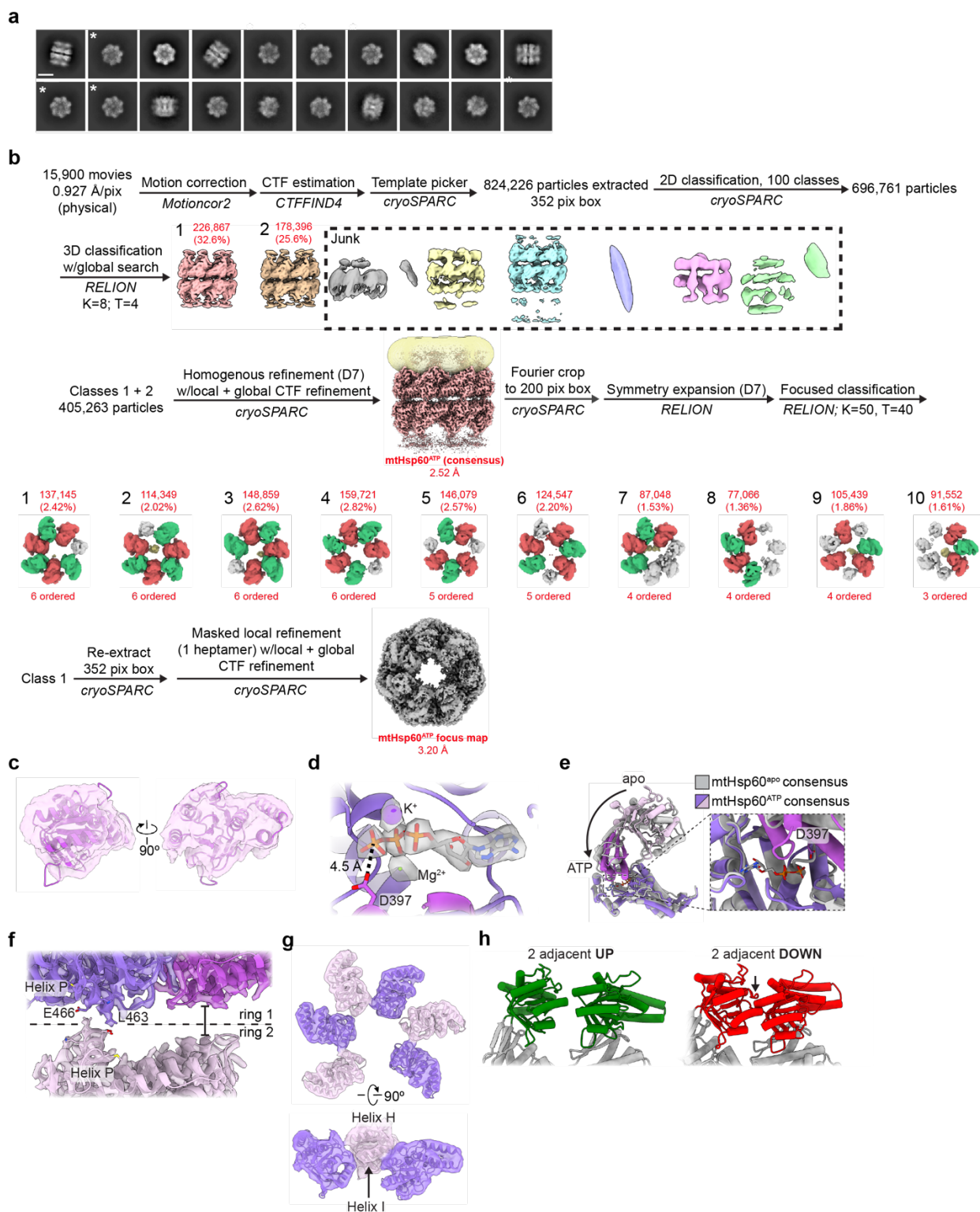
Extended Data Fig. 2

Extended Data Fig. 2. Cryo-EM densities and resolution estimation from the mtHsp60^{V72I} datasets

(**a** to **f**) Fourier Shell Correlation (FSC) curves, orientation distribution plots, sharpened maps colored by local resolution (0.143 cutoff), and map-model FSC curves for (**a**) mtHsp60^{apo} consensus, (**b**) mtHsp60^{apo} focus, (**c**) mtHsp60^{ATP} consensus, (**d**) mtHsp60^{ATP} focus, (**e**) mtHsp60^{ATP}-mtHsp10 consensus, and (**f**) mtHsp60^{ATP}-mtHsp10 focus structures. Displayed model resolutions for map-model FSC plots were determined using the masked map.

33

Extended Data Fig. 3

800

801 **Extended Data Fig. 3. Cryo-EM analysis of ATP-bound mtHsp60^{V72I}**

802 (**a**) Representative 2D class averages from the mtHsp60^{ATP} dataset. Scale bar equals 100 Å.

803 Top views of single ring complexes are indicated (*). (**b**) Cryo-EM processing workflow for

804 structures obtained from the mtHsp60^{ATP} dataset. The mask used for focused classification is

805 shown in transparent yellow with the consensus map. Protomers from focused classification

806 maps are colored in green (apical domain facing upward), red (apical domain facing downward),

807 or gray (disordered apical domain). Class 1 was selected for refinement based on visual

808 assessment of map quality. (**c**) View of an apical domain from the unsharpened mtHsp60^{ATP}

809 consensus map and associated model. (**d**) Nucleotide binding pocket of mtHsp60^{ATP}, showing

810 density for ATP and the γ-phosphate thereof, and Mg^{2+} and K$^+$ ions (gray, from sharpened

811 map). (**e**) Overlay of consensus mtHsp60^{apo} and mtHsp60^{ATP} models, aligned by the equatorial

812 domain, showing a downward rotation of the intermediate and apical domains in the ATP-bound

813 state. (**f**) Inter-ring interface of the sharpened mtHsp60^{ATP} consensus map and fitted model,

814 showing contact at the left interface mediated by helix P, but no contact at the right interface.

815 Each protomer is colored a different shade of purple. (**g**) Unsharpened map and model of apical

816 domains of mtHsp60^{ATP} focus. 'Down' protomers are colored purple, 'up' protomers are colored

817 pink. (**h**) Modeling of two adjacent ATP-bound 'up' (left) or 'down' (right) protomers, generated

818 by aligning a copy of chain C of mtHsp60^{ATP} focus with chain D (up pair) or a copy of chain D

819 with chain C (down pair). A large clash is observed with two adjacent down protomers, while two

820 adjacent up protomers appear compatible.
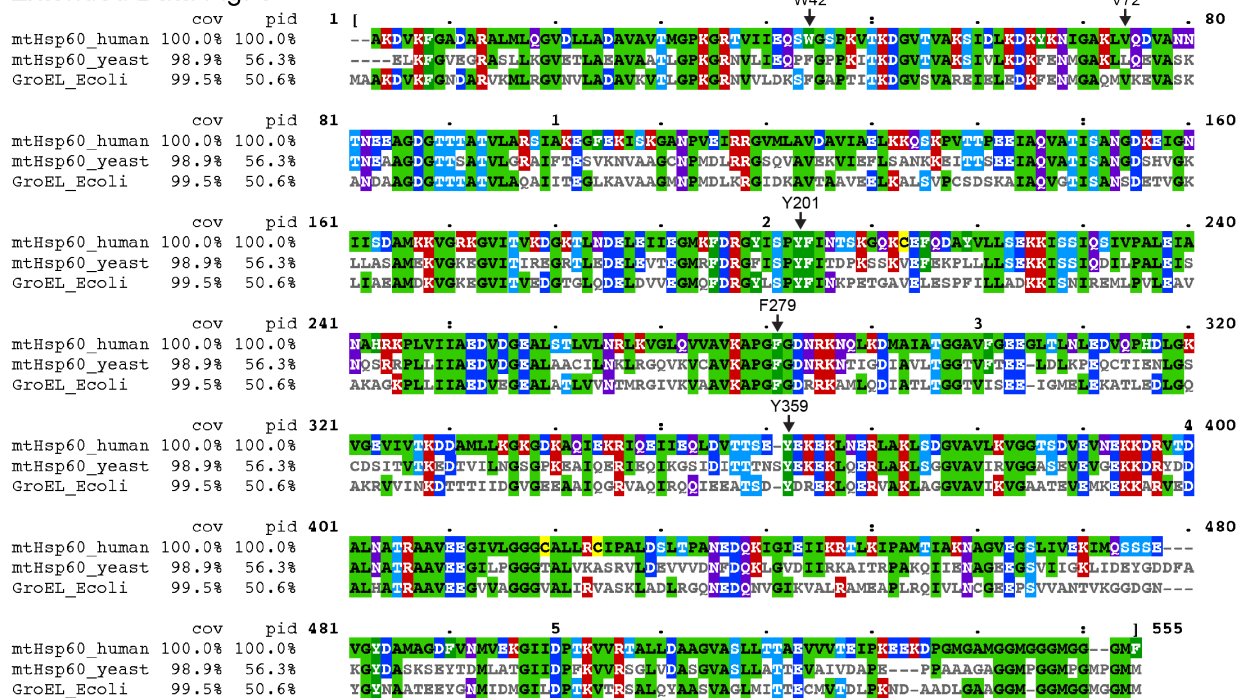
Extended Data Fig. 4
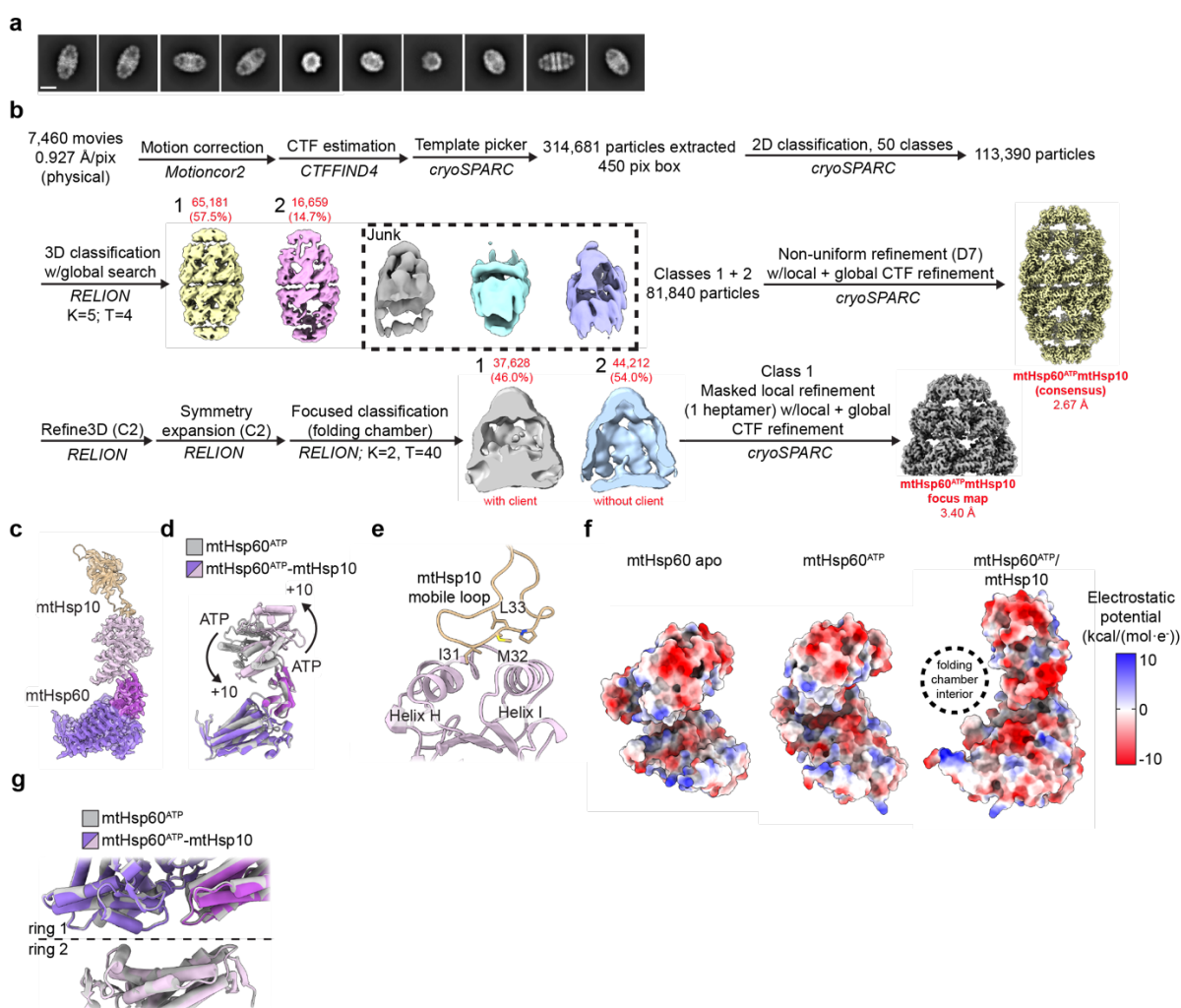
Extended Data Fig. 4. Cryo-EM analysis of ATP/mtHsp10-bound mtHsp60^{V72I}

(**a**) Representative 2D class averages from the mtHsp60^{ATP}-mtHsp10 dataset. Scale bar equals 100 Å. (**b**) Cryo-EM processing workflow for structures obtained from the mtHsp60^{ATP}-mtHsp10 dataset. (**c**) Sharpened map and model for the asymmetric unit of the mtHsp60^{ATP}-mtHsp10 consensus structure. (**d**) Overlay of consensus models for mtHsp60^{ATP} and mtHsp60^{ATP}-mtHsp10 structures, showing identical equatorial and intermediate domain conformations but a large upward apical domain rotation. (**e**) Model of the mtHsp10 mobile loop and associated mtHsp60 apical domain in the mtHsp60^{ATP}-mtHsp10 consensus map, showing interaction of conserved hydrophobic residues with apical domain helices H and I. (**f**) Coulombic potential maps of protomers of mtHsp60 apo, mtHsp60^{ATP}, and mtHsp60^{ATP}-mtHsp10 consensus structures, showing increased negative charge in the inward-facing regions of mtHsp60^{ATP}-mtHsp10. (**g**) Overlay of consensus models for mtHsp60^{ATP} and mtHsp60^{ATP}-mtHsp10 structures, showing highly similar inter-ring conformations.

36

Extended Data Fig. 5

Extended Data Fig. 5. Alignments of group I chaperonin amino acid sequences

Alignments of mature human (residues 27-end) and yeast (*Saccharomyces cerevisiae*, residues 26-end) mitochondrial Hsp60 and *E. coli* GroEL amino acid sequences. Residues mutated in this study are indicated (numbering corresponds to the human sequence). Cov = covariace relative to the human sequence, Pid = percent identity relative to the human sequence.

SUPPLEMENTARY INFORMATION:

Supplementary Video 1. Summary of conformational changes and client contacts in the mtHsp60 reaction cycle

Morphs between mtHsp60^{apo} focus, mtHsp60^{ATP} focus, and mtHsp60^{ATP}-mtHsp10 focus are shown, with experimental client density appearing at each stage. In apo and ATP-bound models helices H and I are colored according to apical domain rotation. For clarity, only one ring of mtHsp60^{ATP} and mtHsp60^{ATP}-mtHsp10 are shown.

37

REFERENCES:

1. Balchin, D., Hayer-Hartl, M., and Hartl, F.U. (2016). In vivo aspects of protein folding and quality control. Science *353*, aac4354. 10.1126/science.aac4354.

2. Horwich, A.L., and Fenton, W.A. (2020). Chaperonin-assisted protein folding: a chronologue. Q Rev Biophys *53*, e4. 10.1017/s0033583519000143.

3. Yébenes, H., Mesa, P., Muñoz, I.G., Montoya, G., and Valpuesta, J.M. (2011). Chaperonins: two rings for folding. Trends Biochem Sci *36*, 424–432. 10.1016/j.tibs.2011.05.003.

4. Lopez, T., Dalton, K., and Frydman, J. (2015). The Mechanism and Function of Group II Chaperonins. J Mol Biol *427*, 2919–2930. 10.1016/j.jmb.2015.04.013.

5. Hayer-Hartl, M., Bracher, A., and Hartl, F.U. (2016). The GroEL–GroES Chaperonin Machine: A Nano-Cage for Protein Folding. Trends Biochem Sci *41*, 62–76. 10.1016/j.tibs.2015.07.009.

6. Fenton, W.A., Kashi, Y., Furtak, K., and Horwich, A.L. (1994). Residues in chaperonin GroEL required for polypeptide binding and release. Nature *371*, 614–619. 10.1038/371614a0.

7. Farr, G.W., Furtak, K., Rowland, M.B., Ranson, N.A., Saibil, H.R., Kirchhausen, T., and Horwich, A.L. (2000). Multivalent Binding of Nonnative Substrate Proteins by the Chaperonin GroEL. Cell *100*, 561–573. 10.1016/s0092-8674(00)80692-3.

8. Elad, N., Farr, G.W., Clare, D.K., Orlova, E.V., Horwich, A.L., and Saibil, H.R. (2007). Topologies of a Substrate Protein Bound to the Chaperonin GroEL. Mol Cell *26*, 415–426. 10.1016/j.molcel.2007.04.004.

9. Weaver, J., Jiang, M., Roth, A., Puchalla, J., Zhang, J., and Rye, H.S. (2017). GroEL actively stimulates folding of the endogenous substrate protein PepQ. Nat Commun *8*, 15934. 10.1038/ncomms15934.

10. Clare, D.K., Vasishtan, D., Stagg, S., Quispe, J., Farr, G.W., Topf, M., Horwich, A.L., and Saibil, H.R. (2012). ATP-Triggered Conformational Changes Delineate Substrate-Binding and -Folding Mechanics of the GroEL Chaperonin. Cell *149*, 113–123. 10.1016/j.cell.2012.02.047.

11. Ranson, N.A., Farr, G.W., Roseman, A.M., Gowen, B., Fenton, W.A., Horwich, A.L., and Saibil, H.R. (2001). ATP-Bound States of GroEL Captured by Cryo-Electron Microscopy. Cell *107*, 869–879. 10.1016/s0092-8674(01)00617-1.

12. Madan, D., Lin, Z., and Rye, H.S. (2008). Triggering Protein Folding within the GroEL-GroES Complex*. J Biol Chem *283*, 32003–32013. 10.1074/jbc.m802898200.

13. Cliff, M.J., Limpkin, C., Cameron, A., Burston, S.G., and Clarke, A.R. (2006). Elucidation of Steps in the Capture of a Protein Substrate for Efficient Encapsulation by GroE. J Biol Chem *281*, 21266–21275. 10.1074/jbc.m601605200.

14. Clare, D.K., Bakkes, P.J., Heerikhuizen, H. van, Vies, S.M. van der, and Saibil, H.R. (2009). Chaperonin complex with a newly folded protein encapsulated in the folding chamber. Nature *457*, 107–110. 10.1038/nature07479.

15. Weissman, J.S., Hohl, C.M., Kovalenko, O., Kashi, Y., Chen, S., Braig, K., Saibil, H.R., Fenton, W.A., and Norwich, A.L. (1995). Mechanism of GroEL action: Productive release of polypeptide from a sequestered position under groes. Cell *83*, 577–587. 10.1016/0092-8674(95)90098-5.

16. Xu, Z., Horwich, A.L., and Sigler, P.B. (1997). The crystal structure of the asymmetric GroEL–GroES–(ADP)7 chaperonin complex. Nature *388*, 741–750. 10.1038/41944.

17. Korobko, I., Eberle, R.B., Roy, M., and Horovitz, A. (2022). A diminished hydrophobic effect inside the GroEL/ES cavity contributes to protein substrate destabilization. Proc National Acad Sci *119*, e2213170119. 10.1073/pnas.2213170119.

18. Weissman, J.S., Rye, H.S., Fenton, W.A., Beechem, J.M., and Horwich, A.L. (1996). Characterization of the Active Intermediate of a GroEL–GroES-Mediated Protein Folding Reaction. Cell *84*, 481–490. 10.1016/s0092-8674(00)81293-3.

19. Neidhardt, F.C., and VanBogelen, R.A. (1981). Positive regulatory gene for temperature-controlled proteins in Escherichia coli. Biochem Bioph Res Co *100*, 894–900. 10.1016/s0006-291x(81)80257-4.

20. Cheng, M.Y., Hartl, F.-U., Martin, J., Pollock, R.A., Kalousek, F., Neuper, W., Hallberg, E.M., Hallberg, R.L., and Horwich, A.L. (1989). Mitochondrial heat-shock protein hsp60 is essential for assembly of proteins imported into yeast mitochondria. Nature *337*, 620–625. 10.1038/337620a0.

21. Manning-Krieg, U.C., Scherer, P.E., and Schatz, G. (1991). Sequential action of mitochondrial chaperones in protein import into the matrix. Embo J *10*, 3273–3280. 10.1002/j.1460-2075.1991.tb04891.x.

22. Itoh, H., Kobayashi, R., Wakui, H., Komatsuda, A., Ohtani, H., Miura, A.B., Otaka, M., Masamune, O., Andoh, H., and Koyama, K. (1995). Mammalian 60-kDa stress protein (chaperonin homolog). Identification, biochemical properties, and localization. J Biol Chem *270*, 13429–13435. 10.1074/jbc.270.22.13429.

23. Beyene, D.A., Naab, T.J., Kanarek, N.F., Apprey, V., Esnakula, A., Khan, F.A., Blackman, M.R., Brown, C.A., and Hudson, T.S. (2018). Differential expression of Annexin 2, SPINK1, and Hsp60 predict progression of prostate cancer through bifurcated WHO Gleason score categories in African American men. Prostate *78*, 801–811. 10.1002/pros.23537.

24. Castilla, C., Congregado, B., Conde, J.M., Medina, R., Torrubia, F.J., Japón, M.A., and Sáez, C. (2010). Immunohistochemical Expression of Hsp60 Correlates With Tumor Progression and Hormone Resistance in Prostate Cancer. Urology *76*, 1017.e1-1017.e6. 10.1016/j.urology.2010.05.045.

25. Hansen, J., Svenstrup, K., Ang, D., Nielsen, M.N., Christensen, J.H., Gregersen, N., Nielsen, J.E., Georgopoulos, C., and Bross, P. (2007). A novel mutation in the HSPD1 gene in a patient with hereditary spastic paraplegia. J Neurol *254*, 897–900. 10.1007/s00415-006-0470-y.

26. Hansen, J.J., Dürr, A., Cournu-Rebeix, I., Georgopoulos, C., Ang, D., Nielsen, M.N., Davoine, C.-S., Brice, A., Fontaine, B., Gregersen, N., et al. (2002). Hereditary Spastic Paraplegia SPG13 Is Associated with a Mutation in the Gene Encoding the Mitochondrial Chaperonin Hsp60. Am J Hum Genetics *70*, 1328–1332. 10.1086/339935.

27. Magen, D., Georgopoulos, C., Bross, P., Ang, D., Segev, Y., Goldsher, D., Nemirovski, A., Shahar, E., Ravid, S., Luder, A., et al. (2008). Mitochondrial Hsp60 Chaperonopathy Causes an Autosomal-Recessive Neurodegenerative Disorder Linked to Brain Hypomyelination and Leukodystrophy. Am J Hum Genetics *83*, 30–42. 10.1016/j.ajhg.2008.05.016.

28. Bross, P., Naundrup, S., Hansen, J., Nielsen, M.N., Christensen, J.H., Kruhøffer, M., Palmfeldt, J., Corydon, T.J., Gregersen, N., Ang, D., et al. (2008). The Hsp60-(p.V98I) Mutation Associated with Hereditary Spastic Paraplegia SPG13 Compromises Chaperonin Function Both *in Vitro* and *in Vivo*. J Biol Chem *283*, 15694–15700. 10.1074/jbc.m800548200.

29. Fontaine, B., Davoine, C.-S., Dürr, A., Paternotte, C., Feki, I., Weissenbach, J., Hazan, J., and Brice, A. (2000). A New Locus for Autosomal Dominant Pure Spastic Paraplegia, on Chromosome 2q24-q34. American Journal of Human Genetics *66*, 702–707.

30. Meng, Q., Li, B.X., and Xiao, X. (2018). Toward Developing Chemical Modulators of Hsp60 as Potential Therapeutics. Frontiers Mol Biosci *5*. 10.3389/fmolb.2018.00035.

31. Nakamura, H., and Minegishi, H. (2013). HSP60 as a Drug Target. Current Pharmaceutical Design *19*, 441–451.

32. Polson, E.S., Kuchler, V.B., Abbosh, C., Ross, E.M., Mathew, R.K., Beard, H.A., Silva, B. da, Holding, A.N., Ballereau, S., Chuntharpursat-Bon, E., et al. (2018). KHS101 disrupts energy metabolism in human glioblastoma cells and reduces tumor growth in mice. Sci Transl Med *10*, eaar2718. 10.1126/scitranslmed.aar2718.

33. Gestwicki, J.E., and Shao, H. (2019). Inhibitors and chemical probes for molecular chaperone networks. J Biol Chem *294*, 2151–2161. 10.1074/jbc.tm118.002813.

34. Brocchieri, L., and Karlin, S. (2008). Conservation among HSP60 sequences in relation to structure, function, and evolution. Protein Sci *9*, 476–486. 10.1110/ps.9.3.476.

35. Klebl, D.P., Feasey, M.C., Hesketh, E.L., Ranson, N.A., Wurdak, H., Sobott, F., Bon, R.S., and Muench, S.P. (2021). Cryo-EM structure of human mitochondrial HSPD1. Iscience *24*, 102022. 10.1016/j.isci.2020.102022.

36. Nisemblat, S., Yaniv, O., Parnas, A., Frolow, F., and Azem, A. (2015). Crystal structure of the human mitochondrial chaperonin symmetrical football complex. Proc National Acad Sci *112*, 6044–6049. 10.1073/pnas.1411718112.

954   37. Gomez-Llorente, Y., Jebara, F., Patra, M., Malik, R., Nisemblat, S., Chomsky-Hecht, O.,
955   Parnas, A., Azem, A., Hirsch, J.A., and Ubarretxena-Belandia, I. (2020). Structural basis for
956   active single and double ring complexes in human mitochondrial Hsp60-Hsp10 chaperonin. Nat
957   Commun *11*, 1916. 10.1038/s41467-020-15698-8.

958   38. Wang, J.C.-Y., and Chen, L. (2021). Structural basis for the structural dynamics of human
959   mitochondrial chaperonin mHsp60. Sci Rep-uk *11*, 14809. 10.1038/s41598-021-94236-y.

960   39. Viitanen, P.V., Lorimer, G., Bergmeier, W., Weiss, C., Kessel, M., and Goloubinoff, P.
961   (1998). [18] Purification of mammalian mitochondrial chaperonin 60 through in Vitro
962   reconstitution of active oligomers. In Methods in Enzymology. (Elsevier), pp. 203–217.

963   40. Miyazaki, T., Yoshimi, T., Furutsu, Y., Hongo, K., Mizobata, T., Kanemori, M., and Kawata,
964   Y. (2002). GroEL-Substrate-GroES Ternary Complexes Are an Important Transient Intermediate
965   of the Chaperonin Cycle*. J Biol Chem *277*, 50621–50628. 10.1074/jbc.m209183200.

966   41. Taniguchi, M., Yoshimi, T., Hongo, K., Mizobata, T., and Kawata, Y. (2004). Stopped-flow
967   Fluorescence Analysis of the Conformational Changes in the GroEL Apical Domain
968   RELATIONSHIPS BETWEEN MOVEMENTS IN THE APICAL DOMAIN AND THE
969   QUATERNARY STRUCTURE OF GroEL*. J Biol Chem *279*, 16368–16376.
970   10.1074/jbc.m311806200.

971   42. Kawata, Y., Kawagoe, M., Hongo, K., Miyazaki, T., Higurashi, T., Mizobata, T., and Nagai, J.
972   (1999). Functional Communications between the Apical and Equatorial Domains of GroEL
973   through the Intermediate Domain †. Biochemistry-us *38*, 15731–15740. 10.1021/bi9909750.

974   43. Chen, L., Syed, A., and Balaji, A. (2022). Hereditary spastic paraplegia SPG13 mutation
975   increases structural stability and ATPase activity of human mitochondrial chaperonin. Sci Rep-
976   uk *12*, 18321. 10.1038/s41598-022-21993-9.

977   44. Gray, T.E., and Fersht, A.R. (1991). Cooperativity in ATP hydrolysis by GroEL is increased
978   by GroES. Febs Lett *292*, 254–258. 10.1016/0014-5793(91)80878-7.

979   45. Bochkareva, E.S., Lissin, N.M., Flynn, G.C., Rothman, J.E., and Girshovich, A.S. (1992).
980   Positive cooperativity in the functioning of molecular chaperone GroEL. J Biol Chem *267*, 6796–
981   6800. 10.1016/s0021-9258(19)50496-3.

982   46. Shao, H., Oltion, K., Wu, T., and Gestwicki, J.E. (2020). Differential scanning fluorimetry
983   (DSF) screen to identify inhibitors of Hsp60 protein–protein interactions. Org Biomol Chem *18*,
984   4157–4163. 10.1039/d0ob00928h.

985   47. Cheng, M.Y., Hartl, F.-U., and Norwich, A.L. (1990). The mitochondrial chaperonin hsp60 is
986   required for its own assembly. Nature *348*, 455–458. 10.1038/348455a0.

987   48. Zhou, M., Li, Y., Hu, Q., Bai, X., Huang, W., Yan, C., Scheres, S.H.W., and Shi, Y. (2015).
988   Atomic structure of the apoptosome: mechanism of cytochrome c- and dATP-mediated
989   activation of Apaf-1. Gene Dev *29*, 2349–2361. 10.1101/gad.272278.115.

990 49. Chen, D.-H., Madan, D., Weaver, J., Lin, Z., Schröder, G.F., Chiu, W., and Rye, H.S. (2013).
991 Visualizing GroEL/ES in the Act of Encapsulating a Folding Protein. Cell *153*, 1354–1365.
992 10.1016/j.cell.2013.04.052.

993 50. Levy-Rimler, G., Viitanen, P., Weiss, C., Sharkia, R., Greenberg, A., Niv, A., Lustig, A.,
994 Delarea, Y., and Azem, A. (2001). The effect of nucleotides and mitochondrial chaperonin 10 on
995 the structure and chaperone activity of mitochondrial chaperonin 60. Eur J Biochem *268*, 3465–
996 3472. 10.1046/j.1432-1327.2001.02243.x.

997 51. Ranson, N.A., Clare, D.K., Farr, G.W., Houldershaw, D., Horwich, A.L., and Saibil, H.R.
998 (2006). Allosteric signaling of ATP hydrolysis in GroEL–GroES complexes. Nat Struct Mol Biol
999 *13*, 147–152. 10.1038/nsmb1046.

1000 52. Tang, Y.-C., Chang, H.-C., Roeben, A., Wischnewski, D., Wischnewski, N., Kerner, M.J.,
1001 Hartl, F.U., and Hayer-Hartl, M. (2006). Structural Features of the GroEL-GroES Nano-Cage
1002 Required for Rapid Folding of Encapsulated Protein. Cell *125*, 903–914.
1003 10.1016/j.cell.2006.04.027.

1004 53. Roh, S.-H., Hryc, C.F., Jeong, H.-H., Fei, X., Jakana, J., Lorimer, G.H., and Chiu, W. (2017).
1005 Subunit conformational variation within individual GroEL oligomers resolved by Cryo-EM. Proc
1006 National Acad Sci *114*, 8259–8264. 10.1073/pnas.1704725114.

1007 54. Zhao, Y., Schmid, M.F., Frydman, J., and Chiu, W. (2021). CryoEM reveals the stochastic
1008 nature of individual ATP binding events in a group II chaperonin. Nat Commun *12*, 4754.
1009 10.1038/s41467-021-25099-0.

1010 55. Farr, G.W., Fenton, W.A., Chaudhuri, T.K., Clare, D.K., Saibil, H.R., and Horwich, A.L.
1011 (2003). Folding with and without encapsulation by cis- and trans-only GroEL–GroES complexes.
1012 Embo J *22*, 3220–3230. 10.1093/emboj/cdg313.

1013 56. Chaudhuri, T.K., Farr, G.W., Fenton, W.A., Rospert, S., and Horwich, A.L. (2001).
1014 GroEL/GroES-Mediated Folding of a Protein Too Large to Be Encapsulated. Cell *107*, 235–246.
1015 10.1016/s0092-8674(01)00523-2.

1016 57. Braig, K., Otwinowski, Z., Hegde, R., Boisvert, D.C., Joachimiak, A., Horwich, A.L., and
1017 Sigler, P.B. (1994). The crystal structure of the bacterial chaperonln GroEL at 2.8 Å. Nature *371*,
1018 578–586. 10.1038/371578a0.

1019 58. Parnas, A., Nadler, M., Nisemblat, S., Horovitz, A., Mandel, H., and Azem, A. (2009). The
1020 MitCHAP-60 Disease Is Due to Entropic Destabilization of the Human Mitochondrial Hsp60
1021 Oligomer. J Biol Chem *284*, 28198–28203. 10.1074/jbc.m109.031997.

1022 59. Viitanen, P.V., Lorimer, G.H., Seetharam, R., Gupta, R.S., Oppenheim, J., Thomas, J.O.,
1023 and Cowan, N.J. (1992). Mammalian Mitochondrial Chaperonin 60 Functions as a Single
1024 Toroidal Ring. Journal of Biological Chemistry *267*, 695–698.

1025 60. Yan, X., Shi, Q., Bracher, A., Miličić, G., Singh, A.K., Hartl, F.U., and Hayer-Hartl, M. (2018).
1026 GroEL Ring Separation and Exchange in the Chaperonin Reaction. Cell *172*, 605-617.e11.
1027 10.1016/j.cell.2017.12.010.

61. Nielsen, K.L., and Cowan, N.J. (1998). A Single Ring Is Sufficient for Productive Chaperonin-Mediated Folding In Vivo. Mol Cell *2*, 93–99. 10.1016/s1097-2765(00)80117-3.

62. Dubaquié, Y., Looser, R., and Rospert, S. (1997). Significance of chaperonin 10-mediated inhibition of ATP hydrolysis by chaperonin 60. Proc National Acad Sci *94*, 9011–9016. 10.1073/pnas.94.17.9011.

63. Mastronarde, D.N. (2005). Automated electron microscope tomography using robust prediction of specimen movements. J Struct Biol *152*, 36–51. 10.1016/j.jsb.2005.07.007.

64. Zheng, S.Q., Palovcak, E., Armache, J.-P., Verba, K.A., Cheng, Y., and Agard, D.A. (2017). MotionCor2: anisotropic correction of beam-induced motion for improved cryo-electron microscopy. Nat Methods *14*, 331–332. 10.1038/nmeth.4193.

65. Rohou, A., and Grigorieff, N. (2015). CTFFIND4: Fast and accurate defocus estimation from electron micrographs. J Struct Biol *192*, 216–221. 10.1016/j.jsb.2015.08.008.

66. Morin, A., Eisenbraun, B., Key, J., Sanschagrin, P.C., Timony, M.A., Ottaviano, M., and Sliz, P. (2013). Collaboration gets the most out of software. Elife *2*, e01456. 10.7554/elife.01456.

67. Punjani, A., Rubinstein, J.L., Fleet, D.J., and Brubaker, M.A. (2017). cryoSPARC: algorithms for rapid unsupervised cryo-EM structure determination. Nat Methods *14*, 290–296. 10.1038/nmeth.4169.

68. Scheres, S.H.W. (2012). RELION: Implementation of a Bayesian approach to cryo-EM structure determination. J Struct Biol *180*, 519–530. 10.1016/j.jsb.2012.09.006.

69. Croll, T.I. (2018). ISOLDE: a physically realistic environment for model building into low-resolution electron-density maps. Acta Crystallogr Sect D Struct Biology *74*, 519–530. 10.1107/s2059798318002425.

70. Emsley, P., Lohkamp, B., Scott, W.G., and Cowtan, K. (2010). Features and development of Coot. Acta Crystallogr Sect D Biological Crystallogr *66*, 486–501. 10.1107/s0907444910007493.

71. Madeira, F., Pearce, M., Tivey, A.R.N., Basutkar, P., Lee, J., Edbali, O., Madhusoodanan, N., Kolesnikov, A., and Lopez, R. (2022). Search and sequence analysis tools services from EMBL-EBI in 2022. Nucleic Acids Res *50*, W276–W279. 10.1093/nar/gkac240.

72. Afonine, P.V., Poon, B.K., Read, R.J., Sobolev, O.V., Terwilliger, T.C., Urzhumtsev, A., and Adams, P.D. (2018). Real-space refinement in PHENIX for cryo-EM and crystallography. Acta Crystallogr Sect D Struct Biology *74*, 531–544. 10.1107/s2059798318006551.

73. Pettersen, E.F., Goddard, T.D., Huang, C.C., Couch, G.S., Greenblatt, D.M., Meng, E.C., and Ferrin, T.E. (2004). UCSF Chimera—A visualization system for exploratory research and analysis. J Comput Chem *25*, 1605–1612. 10.1002/jcc.20084.

1062   74. Pettersen, E.F., Goddard, T.D., Huang, C.C., Meng, E.C., Couch, G.S., Croll, T.I., Morris,
1063   J.H., and Ferrin, T.E. (2021). UCSF ChimeraX: Structure visualization for researchers,
1064   educators, and developers. Protein Sci *30*, 70–82. 10.1002/pro.3943.

1065   75. Chang, L., Bertelsen, E.B., Wisén, S., Larsen, E.M., Zuiderweg, E.R.P., and Gestwicki, J.E.
1066   (2008). High-throughput screen for small molecules that modulate the ATPase activity of the
1067   molecular chaperone DnaK. Anal Biochem *372*, 167–176. 10.1016/j.ab.2007.08.020.